ITCZ Breakdown and Its Upscale Impact on the Planetary-Scale Circulation over the Eastern Pacific

Yang, Q., Majda, A. J., & Khouider, B.

2017

This article was originally published at:
https://doi.org/10.1175/JAS-D-17-0021.1

ITCZ Breakdown and Its Upscale Impact on the Planetary-Scale Circulation over the Eastern Pacific

QIU YANG AND ANDREW J. MAJDA

Department of Mathematics, and Center for Atmosphere Ocean Science, Courant Institute of Mathematical Sciences, New York University, New York, New York, and Center for Prototype Climate Modeling, New York University Abu Dhabi, Abu Dhabi, United Arab Emirates

BOUALEM KHOUIDER

Department of Mathematics and Statistics, University of Victoria, Victoria, British Columbia, Canada

(Manuscript received 22 January 2017, in final form 11 September 2017)

ABSTRACT

The eastern Pacific (EP) intertropical convergence zone (ITCZ) is sometimes observed to break down into several vortices on the synoptic time scale. It is still a challenge for present-day numerical models to simulate the ITCZ breakdown in the baroclinic modes. Also, the upscale impact of the associated mesoscale fluctuations on the planetary-scale circulation is not well understood. Here, a simplified multiscale model for the modulation of the ITCZ is used to study these issues. A prescribed two-scale heating drives the planetary-scale circulation through both planetary-scale mean heating and eddy flux divergence of zonal momentum, where the latter represents the upscale impact of mesoscale disturbances. In an idealized scenario where the heating only varies on the mesoscale, key features of the ITCZ breakdown in the baroclinic modes are captured. The eddy flux divergence of zonal momentum is characterized by midlevel (low level) eastward (westward) momentum forcing at subtropical latitudes of the Northern Hemisphere and opposite-signed midlevel momentum forcing at low latitudes. Such upscale impact of mesoscale fluctuations tends to accelerate (decelerate) planetary-scale zonal jets in the middle (lower) troposphere. Compared with deep heating, shallow heating induces stronger vorticity anomalies on the mesoscale and more significant eddy flux divergence of zonal momentum and acceleration–deceleration effects on the planetary-scale mean flow. In a more realistic scenario where the heating also varies on the planetary scale, the most significant zonal velocity anomalies are confined in the diabatic heating region.

1. Introduction

The intertropical convergence zone (ITCZ) is a narrow band of cloudiness encircling Earth in the tropics. With the advent of high-resolution satellite measurement, global-scale analysis for the ITCZ has provided the scientific community concise descriptions of global ITCZ climatology (Waliser and Gautier 1993). In particular, while in most parts of the tropics, the ITCZ migrates back and forth with the seasonal cycle, following the summer hemisphere, the eastern Pacific (EP) ITCZ remains in the Northern Hemisphere along the latitudes between 5° and 15°N all year-round. This has attracted the attention of the community. Many theoretical and numerical studies have been undertaken to understand the underlying mechanisms (Philander et al. 1996), but climate models fail to capture this phenomenon, which is associated with the so-called double-ITCZ problem (Hubert et al. 1969; Zhang 2001; Lin 2007).

Instead of being a steady state, the EP ITCZ is observed to sometimes undulate and break down on the synoptic time scale (Ferreira and Schubert 1997). In details, the ITCZ first undulates and breaks down into several mesoscale disturbances in the form of displaced cloud clusters at different locations. Among these disturbances, some grow to become tropical cyclones and others dissipate in the following several days. As tropical cyclones move to high latitudes, a new ITCZ band of cloudiness reforms in the original place. This whole process, referred to as the ITCZ breakdown, can significantly impact the local weather and global atmospheric conditions

Denotes content that is immediately available upon publication as open access.

Corresponding author: Qiu Yang, yangq@cims.nyu.edu

DOI: 10.1175/JAS-D-17-0021.1

(Gray 1979), and many physical mechanisms have been proposed to explain the ITCZ breakdown (Wang and Magnusdottir 2006). For instance, easterly waves (Toma and Webster 2010a,b) are thought to provide an external precursor for the ITCZ breakdown when these westward-moving synoptic-scale disturbances propagate to the EP and disturb the ITCZ flow field (Gu and Zhang 2002). Internal instabilities such as the vortex roll-up mechanism (Hack et al. 1989; Ferreira and Schubert 1997), due to the persistence of a reversed meridional potential vorticity gradient field, are also proposed to explain the ITCZ breakdown.

While these theories provide plausible ways through which mesoscale disturbances can be generated during the ITCZ breakdown, simulations in idealized model setup show encouraging, but far from satisfactory, results. The barotropic aspects of the ITCZ breakdown have been examined through a nonlinear shallow water model on the sphere (Ferreira and Schubert 1997). After prescribing a zonally elongated mass sink near the equator, a potential vorticity strip with a reversed meridional gradient appears on the poleward side of the mass sink, which is unstable with weak disturbances and resembles the ITCZ breakdown. However, the baroclinic aspects of the ITCZ breakdown are not captured by the shallow-water model in Ferreira and Schubert (1997). On the other hand, three-dimensional simulations using a primitive-equation model have been used to model the atmospheric flows during the ITCZ breakdown (Wang and Magnusdottir 2005). The potential vorticity strip, forced by thermal forcing in the first 5 days, undulates and breaks down into vorticity anomalies, resembling the tropical cyclones, over several hundred kilometers in the EP ITCZ.

The EP ITCZ is a region of intense convection where both shallow and deep convection take place, but the role of the associated convective flows in the ITCZ breakdown and their upscale impact on the planetary-scale circulation has not yet been determined; besides deep meridional circulation in the EP ITCZ, shallow meridional circulation with northerly returning flows just above the atmospheric boundary layer (ABL) is observed by satellite measurement and dropsondes and wind profilers (Zhang et al. 2004; Nolan et al. 2007; Zhang et al. 2008). The goals of this paper are as follows: first, using a simple multiscale model to simulate flow fields in the baroclinic modes when the ITCZ breakdown occurs; second, assessing upscale impact of the associated mesoscale fluctuations on the planetary-scale circulation, through eddy flux divergence of zonal momentum; and third, discussing how such upscale impact is influenced by the depth of diabatic heating, including shallow congestus heating and deep convective heating.

Self-consistent multiscale models based on multiscale asymptotic methods were derived systematically and used to describe the hierarchical structures of atmospheric flows in the tropics (Majda and Klein 2003; Majda 2007). The advantages of using these multiscale models lie in isolating the essential components of multiscale interaction and providing direct assessment of the upscale impact of the small-scale fluctuations onto the large-scale mean flow, through eddy flux divergence of momentum and temperature. In particular, the modulation of the ITCZ (M-ITCZ) equations (Biello and Majda 2013) describe atmospheric flows on both the mesoscale and planetary scale, which are the typical scales of atmospheric flows in the EP ITCZ.

Instead of considering possible instability mechanisms for the ITCZ breakdown as Ferreira and Schubert (1997) and Wang and Magnusdottir (2005), here we are using this simple multiscale model to simulate flow fields driven by a prescribed heating, which is used to mimic latent heat release when the ITCZ breakdown occurs. In this paper, we demonstrate how convective heating, occurring at the mesoscale and from both shallow and deep convection, can induce the modulation of a positive vorticity strip and formation of a strong vortex. We begin with an idealized scenario of a zonally symmetric planetary-scale flow. A zonally localized heating is prescribed, on the mesoscale, in the Northern Hemisphere to mimic diabatic heating associated with cloud clusters in the EP ITCZ. Outside this heating region, horizontally uniform cooling is assumed, to mimic radiative cooling and subsiding motion in the cold and dry regions (Toma and Webster 2010a). Both deep convective heating and shallow congestus heating are used here in the M-ITCZ equations, and the resulting mesoscale solutions are compared in terms of their different upscale impact. In fact, the deep and shallow ITCZ breakdown classified by convection depth have been observed and studied in Wang and Magnusdottir (2006). Then a more realistic scenario with a zonally varying planetary-scale flow is considered, where the diabatic heating is modulated by a convective envelope to mimic the EP ITCZ.

The M-ITCZ equations are initialized from a background state of rest and numerically integrated when forced by the diabatic heating. The baroclinic aspects of the ITCZ breakdown are examined in terms of the spatial pattern of vorticity and flow fields. In the deep heating case, the eddy flux divergence of zonal momentum is characterized by midlevel (low level) eastward (westward) momentum forcing at subtropical latitudes of the Northern Hemisphere and opposite-signed midlevel momentum forcing at low latitudes. By investigating the kinetic energy budget, it is found that

the eddy impact of the mesoscale dynamics accelerate midlevel zonal jets at both low and subtropical latitudes and decelerate low-level zonal jets at subtropical latitudes. Furthermore, compared with deep convective heating, with the same maximum heating magnitude, shallow congestus heating is found to drive stronger vorticity anomalies and induces more significant eddy flux divergence of zonal momentum and acceleration–deceleration effects in the Northern Hemisphere. In the more realistic scenario of a large-scale modulated mesoscale heating, we found that the most significant zonal velocity anomalies are confined to the diabatic heating region, while small zonal velocity anomalies are transported away by the planetary-scale gravity waves.

The rest of this paper is organized as follows: The properties of the M-ITCZ equations are discussed in section 2. Section 3 presents numerical solutions for the ITCZ breakdown in zonally symmetric planetary-scale flow. Both deep convective heating and shallow congestus heating cases are considered in the same model setup and compared in terms of vorticity field, eddy flux divergence of zonal momentum, and acceleration–deceleration effects on the mean flow. Section 4 considers the scenario in zonally varying planetary-scale flow. The paper ends with a concluding discussion. The numerical scheme for solving the M-ITCZ equations is summarized in the appendix.

2. Properties of the M-ITCZ equations

a. The governing equations

Inspired by the multiscale features of tropical convection, the multiscale asymptotic methods were used to derive reduced models across multiple spatiotemporal scales (Majda and Klein 2003; Majda 2007). In particular, the M-ITCZ equations, derived in Biello and Majda (2013), describe the multiscale dynamics of the ITCZ from the diurnal to monthly time scales in which mesoscale convectively coupled Rossby waves are modulated by large-scale gravity waves. To derive this multiscale model, two zonal length scales (planetary-scale $X = \varepsilon x$ and mesoscale x) are introduced, where the Froude number ε, considered as a small parameter, is used for asymptotic expansion. Here, the Froude number is taken to be 0.1. Then the original zonal derivatives are replaced by their multiscale counterparts,

$$\frac{\partial}{\partial x} \to \frac{\partial}{\partial x} + \varepsilon \frac{\partial}{\partial X}, \tag{1}$$

and all physical variables have the following asymptotic expansion:

$$u^{\varepsilon}(X,x,y) = u(X,x,y) + \varepsilon u_1(X,x,y), \tag{2}$$

$$v^{\varepsilon}(X,x,y) = v(X,x,y) + \varepsilon v_1(X,x,y), \tag{3}$$

$$w^{\varepsilon}(X,x,y) = w(X,x,y) + \varepsilon W(X), \tag{4}$$

$$\theta^{\varepsilon}(X,x,y) = \varepsilon^{-1}\Theta(X) + \theta(X,x,y), \tag{5}$$

$$p^{\varepsilon}(X,x,y) = \varepsilon^{-1}\Pi(X) + p(X,x,y), \tag{6}$$

where all variables also depend on height z and time t. The M-ITCZ model is derived by collecting the terms from the same order of ε in the framework of the multiscale asymptotics. The M-ITCZ equations in dimensionless units read as follows:

$$\frac{Du}{Dt} - yv = -\frac{\partial p}{\partial x} - \frac{\partial \Pi}{\partial X} - du, \tag{7a}$$

$$\frac{Dv}{Dt} + yu = -\frac{\partial p}{\partial y} - dv, \tag{7b}$$

$$w = S_{\theta}, \tag{7c}$$

$$\frac{\partial u}{\partial x} + \frac{\partial v}{\partial y} + \frac{\partial w}{\partial z} = 0, \tag{7d}$$

$$\frac{\partial \Pi}{\partial z} = \Theta, \tag{7e}$$

$$\frac{\partial \Theta}{\partial t} + \langle \overline{w} \rangle \frac{\partial \Theta}{\partial z} + W = 0, \tag{7f}$$

$$\frac{\partial}{\partial X}(\langle \overline{u} \rangle - U) + \frac{\partial W}{\partial z} = 0, \tag{7g}$$

where $D/Dt = \partial/\partial t + u\partial/\partial x + v\partial/\partial y + w\partial/\partial z$ is the advection derivative due to the three-dimensional flow. The barotropic component of the mesoscale mean zonal velocity U is denoted

$$U(X,t) \equiv \frac{1}{\pi}\int_0^{\pi} \langle \overline{u} \rangle (X,z,t)dz \tag{8}$$

where the depth of the troposphere is set as π in dimensionless units. The mesoscale zonal and meridional averaging operators for an arbitrary function f are defined as follows:

$$\overline{f}(X,y,z,t) = \lim_{L\to\infty} \frac{1}{2L}\int_{-L}^{L} f(x,X,y,z,t)dx, \tag{9}$$

$$\langle f \rangle (x,X,z,t) = \frac{1}{2L_*}\int_{-L_*}^{L_*} f(x,X,y,z,t)dy, \tag{10}$$

where L is the mesoscale zonal length of the domain and taken to be infinity in the asymptotic limit. Practically, such an extreme requirement is relaxed and a relatively large value of L is chosen. In Eq. (10) L_* measures the finite poleward extent of the domain on the equatorial β plane. The domain has finite extent in both the meridional and vertical directions and is periodic in the zonal direction, resembling the tropical belt.

Equations (7a) and (7b) are, respectively, the zonal and meridional momentum equations on an equatorial β plane, where u and v are the zonal and meridional velocity depending on both the mesoscale zonal, meridional, and temporal coordinate variables x, y, and t and the planetary-scale zonal coordinate X. The terms on the right-hand side are the gradients of the mesoscale and planetary-scale pressure p and Π, respectively, and momentum damping with a vertically varying damping time scale $1/d$. Equation (7c) is the thermal equation satisfying the weak temperature gradient assumption (Sobel et al. 2001), which assumes that vertical velocity w is directly determined by diabatic heating S_θ. Equation (7d) is the continuity equation for the three-dimensional mesoscale flows. Equation (7e) denotes the hydrostatic balance between planetary-scale pressure Π and potential temperature anomalies Θ, where the former has no dependence on the mesoscale zonal and meridional coordinates. Equation (7f) is the thermal equation involving planetary-scale potential temperature anomalies Θ and planetary-scale vertical velocity W. The mesoscale horizontal average of vertical velocity $\langle \overline{w} \rangle$ is directly specified by diabatic heating S_θ through Eq. (7f). Equation (7g) is the continuity equation for the two-dimensional planetary-scale flows, including planetary-scale zonal velocity in the baroclinic modes and planetary-scale vertical velocity. The linear momentum damping terms $-du$ and $-dv$ are used to mimic cumulus drag in large-scale tropical flows (Lin et al. 2005).

As suggested by the dimensionless relation, $X = \varepsilon x$, the ratio between mesoscale and planetary scale has the same value as the Froude number ε. For practical reasons, a small value of Froude number, $\varepsilon = 0.1$, is specified here. Except for the large-scale pressure gradient $-\Pi_X$ in Eq. (7a), the first four equations in Eqs. (7a)–(7d) govern tropical flows on the mesoscale, where one dimensionless unit of (x, y) corresponds to 500 km and those of horizontal and vertical velocities correspond to 5 and 0.05 m s^{-1}, respectively. The diabatic heating S_θ measured in units of 33 K day^{-1} directly drives the mesoscale dynamics in weak temperature gradient balance. Equations (7e)–(7g) describe the zonal modulation of tropical flows on the planetary scale, where one dimensionless unit of X corresponds to 5000 km and potential temperature anomalies Θ and planetary-scale vertical velocity W are measured in units of 3.3 K and 0.005 m s^{-1}, respectively. When coupled with the mesoscale-mean zonal velocity and planetary-scale pressure gradient in Eq. (7a), the last three equations describe planetary-scale gravity waves propagating zonally in the tropics.

b. *Mesoscale barotropic Rossby waves and planetary-scale gravity waves*

One crucial feature of the M-ITCZ equations is that the planetary-scale and mesoscale dynamics are nonlinearly coupled with each other. Such a model with complete nonlinearity is quite different from other multiscale models (Biello and Majda 2005, 2006; Majda 2007; Biello and Majda 2010; Majda et al. 2010; Yang and Majda 2014; Majda and Yang 2016). In those models, the flow fields on different scales are governed by different groups of equations and the scale interactions are explicitly expressed in eddy flux divergences of momentum and temperature.

Although both the planetary-scale and mesoscale dynamics in the M-ITCZ equations are completely coupled to each other, the mesoscale dynamics can still be isolated by assuming zonal symmetry (i.e., X independence) of the planetary-scale dynamics. Then the equations for the mesoscale dynamics in dimensionless units are just the first four equations in Eqs. (7a)–(7d) without zonal gradient of planetary-scale pressure $-\Pi_X$, which are called mesoscale equatorial weak temperature gradient (MEWTG) equations (Majda and Klein 2003). The MEWTG equations have been applied to model a variety of physical phenomena in the tropical circulation such as the hurricane embryo (Majda et al. 2008, 2010).

The equations for planetary-scale gravity waves in dimensionless units read as follows:

$$\frac{\partial \overline{u}}{\partial t} + \frac{\partial}{\partial y}(\overline{v}\,\overline{u}) + \frac{\partial}{\partial z}(\overline{w}\,\overline{u}) - y\overline{v} = -\frac{\partial \Pi}{\partial X} - d\overline{u} - \frac{\partial}{\partial y}(\overline{v'u'}) - \frac{\partial}{\partial z}(\overline{w'u'}), \tag{11a}$$

$$\overline{w} = \overline{S}_\theta, \tag{11b}$$

$$\frac{\partial \overline{v}}{\partial y} + \frac{\partial \overline{w}}{\partial z} = 0, \tag{11c}$$

where the prime notation denotes mesoscale zonal fluctuations $f = \overline{f} + f'$, satisfying $\overline{f'} = 0$. The planetary-scale circulation in Eqs. (11a)–(11c) feeds both upscale impact of mesoscale fluctuations through eddy flux divergence of zonal momentum and also momentum damping, which can be learned by taking mesoscale zonal averaging of Eqs. (7a), (7c), and (7d). The mesoscale zonal average of Eq. (7b) for meridional momentum involves meridional gradient of pressure term on its right-hand side $-\overline{p}_y$ and serves as a diagnostic equation for $\overline{p}$. Thus, it is not included here. In fact, the zonal-mean meridional velocity $\overline{v}$ is directly determined through Eqs. (11b) and (11c). Equations (11a)–(11c) are also coupled with Eqs. (7e)–(7g) involving planetary-scale

pressure Π, potential temperature anomalies Θ, and planetary-scale vertical velocity W.

Equations (11a)–(11c) and (7e)–(7g) describe zonally propagating gravity waves on the planetary scale. In fact, the planetary-scale gravity wave equations without upscale fluxes have been studied in Biello and Majda (2013). The planetary-scale gravity waves tend to equalize the meridional mean of the vertical shear of zonal wind at all longitudes in the tropics. Meanwhile, they carry cold temperature anomalies and upward velocity to the west, providing favorable conditions for convection in a moist environment. The east–west asymmetry is induced by the β effect because of the two-way coupling between mesoscale and planetary-scale dynamics, as appears in the governing equations for planetary-scale circulation in Eqs. (11a)–(11c) (Biello and Majda 2013).

c. *Conservation of potential vorticity and kinetic energy*

In the M-ITCZ equations, the planetary-scale gravity wave dynamics does not directly modify the potential vorticity (PV) on the mesoscale except for the advection by the mean zonal velocity. The equation for PV, Q, is given by

$$\frac{DQ}{Dt} = Q\frac{\partial S_\theta}{\partial z} - \frac{\partial v}{\partial z}\frac{\partial S_\theta}{\partial x} + \frac{\partial u}{\partial z}\frac{\partial S_\theta}{\partial y} - d\omega, \tag{12}$$

where $Q = \omega + y$ and $\omega = v_x - u_y$ is the relative vorticity. Instead of being materially conserved, Q responds directly to diabatic heating through the terms on the right-hand side of Eq. (12), including vortex stretching, $Q\partial S_\theta/\partial z$, vortex tilting, $-(\partial v/\partial z)(\partial S_\theta/\partial x) + (\partial u/\partial z)(\partial S_\theta/\partial y)$, and vorticity damping $-d\omega$.

The conservation of the mesoscale kinetic energy $K_m = (u^2 + v^2)/2$ is given by

$$\frac{\partial K_m}{\partial t} + \nabla\cdot(K_m\mathbf{v} + p\mathbf{u}) = -pw_z - \frac{\partial \Pi}{\partial X}u - 2dK_m, \tag{13}$$

where $\mathbf{v} = (u, v, w)$ represents the three-dimensional velocity field and $\mathbf{u} = (u, v, 0)$ is the horizontal velocity field. In Eq. (13), the kinetic energy density $\partial K_m/\partial t$ is balanced by the divergence of the energy flux, $\nabla\cdot(K_m\mathbf{v} + p\mathbf{u})$, in a conservation form on the right-hand side and modified by the sources and sinks of energy on the right-hand side. The term $-pw_z$ is a kinetic energy source. Suppose there is deep heating in the mesoscale domain, the resulting upward motion tends to induce positive (negative) gradient of vertical motion and low (high) pressure in the lower (upper) troposphere, generating kinetic energy transfer from the diabatic heating. The term $-(\partial\Pi/\partial X)u$ can be either kinetic energy source or sink, depending on the directions of planetary-scale pressure gradient and zonal velocity. The term $-2dK_m$ is a kinetic energy sink due to cumulus drag.

The equation for the planetary-scale kinetic energy $K = (\overline{u}^2 + \overline{v}^2)/2$ is given by

$$\frac{\partial K}{\partial t} + \frac{\partial}{\partial y}(\overline{v}K) + \frac{\partial}{\partial z}(\overline{w}K) = -\frac{\partial \Pi}{\partial X}\overline{u} - \frac{\partial \overline{p}}{\partial y}\overline{v} - 2dK + F^u\overline{u} + F^v\overline{v}, \tag{14}$$

where $F^u = -(\overline{v'u'})_y - (\overline{w'u'})_z$ and $F^v = -(\overline{v'v'})_y - (\overline{w'v'})_z$ are the eddy flux divergence of momentum from the mesoscale fluctuations. From Eq. (14), the change of kinetic energy density is balanced by the divergence of energy flux and several forcing terms on the right-hand side. In detail, the kinetic energy flux term $(\overline{v}K)_y + (\overline{w}K)_z$ represents the advection effect of the planetary-scale meridional–vertical circulation $(\overline{v}, \overline{w})$. On the right-hand side, the first term $-\Pi_X\overline{u}$ represents the acceleration–deceleration effects of large-scale pressure gradient in zonal direction. The second term $-\overline{p}_y\overline{v}$ represents the acceleration–deceleration effects of pressure gradient in meridional direction. The third term $-2dK$ is the energy dissipation due to cumulus drag. The last two terms, $F^u\overline{u}$ and $F^v\overline{v}$, denote the acceleration–deceleration effects due to mesoscale eddy flux divergence of zonal and meridional momentum.

3. Upscale impact of mesoscale fluctuations driven by prescribed mesoscale heating

To model ITCZ breakdown in a simple scenario, the solutions of the M-ITCZ equations are assumed to be zonally symmetric on the planetary scale so that all derivatives about planetary-scale X vanish. Then the M-ITCZ equations [Eqs. (7a)–(7g)] are reduced to the MEWTG equations, where S_θ stands for thermal forcing such as diabatic heating in cloud clusters and radiative cooling effects.

For simplicity, local periodicity is imposed in mesoscale zonal direction and rigid boundary conditions are imposed in meridional and vertical boundaries. Consequently, an implicit constraint for diabatic heating can be derived and applies to each height level z,

$$\langle \overline{S}_\theta \rangle = 0, \tag{15}$$

where the overbar and angle brackets stand for mesoscale zonal and meridional averaging as defined in Eqs. (9) and (10). The localized mesoscale heating here is used to mimic a mesoscale convective system that evolves inside the ITCZ background. This system will then produce eddy fluxes that would affect the planetary-scale flow associated with the ITCZ. The goal

TABLE 1. Details about the size of the multiscale domain with nested coarse and fine grids, grid number, grid spacing, total time, and time steps in the numerical simulations.

Name	Value	Name	Value	Name	Value
Zonal length of the planetary-scale domain	4×10^4 km	Coarse X-grid number	41	X-grid spacing	0.976×10^3 km
Zonal length of the mesoscale domain	0.976×10^3 km	Fine x-grid number	81	x-grid spacing	12.045 km
Meridional length of the domain	3×10^3 km	y-grid number	241	y-grid spacing	12.5 km
Vertical length of the domain	15.7 km	z-grid number	127	z-grid spacing	0.125 km
Total time	4 days	Number of time steps	1200	Time step size	4.8 min

here is to understand what kind of upscale impact is going to emerge from a localized mesoscale heating.

The momentum dissipation for cumulus drag is described by a linear damping law. The coefficient d (day^{-1}) sets the time scale for momentum dissipation on the mesoscale. According to the observation, momentum damping time scale at the surface of the Pacific Ocean could be as strong as 1 day (Deser 1993), while that at the upper troposphere is much longer. In general, the momentum damping of large-scale circulation occurs on a time scale O(1–10) days and also depends on the vertical wavelength of the wind profile (Romps 2014). For simplicity, here, the momentum damping coefficient d is assumed to be a linear function of height $d(z)$, which has 1-day damping time scale at surface and 10-day damping time scale at top of the troposphere.

The MEWTG equations are solved numerically by using a new method based on the Helmholtz decomposition and a second-order corner transport upwind scheme to effectively resolve the nonlinear eddies. The details of the numerical scheme are summarized in the appendix.

For the numerical simulations in sections 3 and 4, the banded region from 15°S to 15°N circling the globe in the tropics is chosen as the full domain with zonal extent $0 \le X \le 40 \times 10^3$ km. As summarized in the appendix, the coarse grid number N_{xp} is fixed and the zonal extent of each mesoscale box is 0.976×10^3 km. In the numerical scheme with nested grids, each coarse cell corresponds to a single mesoscale box with a horizontal extent of $0 \le x \le 0.976 \times 10^3$ km, $-1.5 \times 10^3 \le y \le 1.5 \times 10^3$ km and a vertical extent of $0 \le z \le 15.7$ km. Besides, the planetary-scale domain and all mesoscale domains share the same vertical grids. The details about grid numbers and grid spacing in the numerical simulations are summarized in Table 1 and section 4.

a. Deep and shallow heating profile

The dominating meridional circulation over the EP consists of a strong overturning circulation cell around the equator and a weak one at subtropical latitudes of the Northern Hemisphere. Such a deep overturning cell can be explained as the response of the large-scale circulation to deep convective heating in the ITCZ (Schneider and Lindzen 1977; Wu 2003). The deep convective heating in the ITCZ comes from latent heat release during precipitation associated with cloudiness such as deep convective cumulonimbus clouds, which tends to warm and dry the entire troposphere and produce amounts of rainfall.

Here, the deep convective heating S_θ for a single cloud cluster in dimensionless units is prescribed as follows:

$$S_\theta = cH(x,y)G(z)\phi(t), \tag{16}$$

where heating magnitude coefficient $c = 2$ corresponds to the maximum heating rate of 66 K day^{-1}; $H(x, y)$ is the horizontal envelope function shown in Fig. 1a. The vertical heating profile is the first baroclinic mode $G(z) = \sin(z)$, as shown in Fig. 1c. The time-dependent heating magnitude linearly increases from 0 to 1 at day 1 and remains constant afterward. Since the typical lifetime of cloud clusters is between several hours and several days (Mapes and Houze 1993), here, 1 day in duration is set as initialization time when the deep convective heating increases from zero to its maximum magnitude. As shown in Fig. 1a, the deep heating is located at the latitudes between $y = 0$ and 1.2×10^3 km of the Northern Hemisphere and zonally localized in the center of the mesoscale domain. Outside of the convective heating region, there is horizontally uniform cooling in much weaker magnitude, which is used to mimic radiative cooling in the troposphere (Toma and Webster 2010a).

In general, large-scale meridional circulation in the tropics can be regarded as a response to convective heating (Schneider and Lindzen 1977; Gill 1980; Wu 2003). The large-scale circulation response to deep convective heating is a deep overturning cell, while that to shallow convective heating is a shallow overturning cell with its upper-branch northerly winds above the ABL. Here, the shallow congestus heating S_θ in dimensionless units is prescribed in the same general expression in Eq. (16) and heating magnitude coefficient c_s

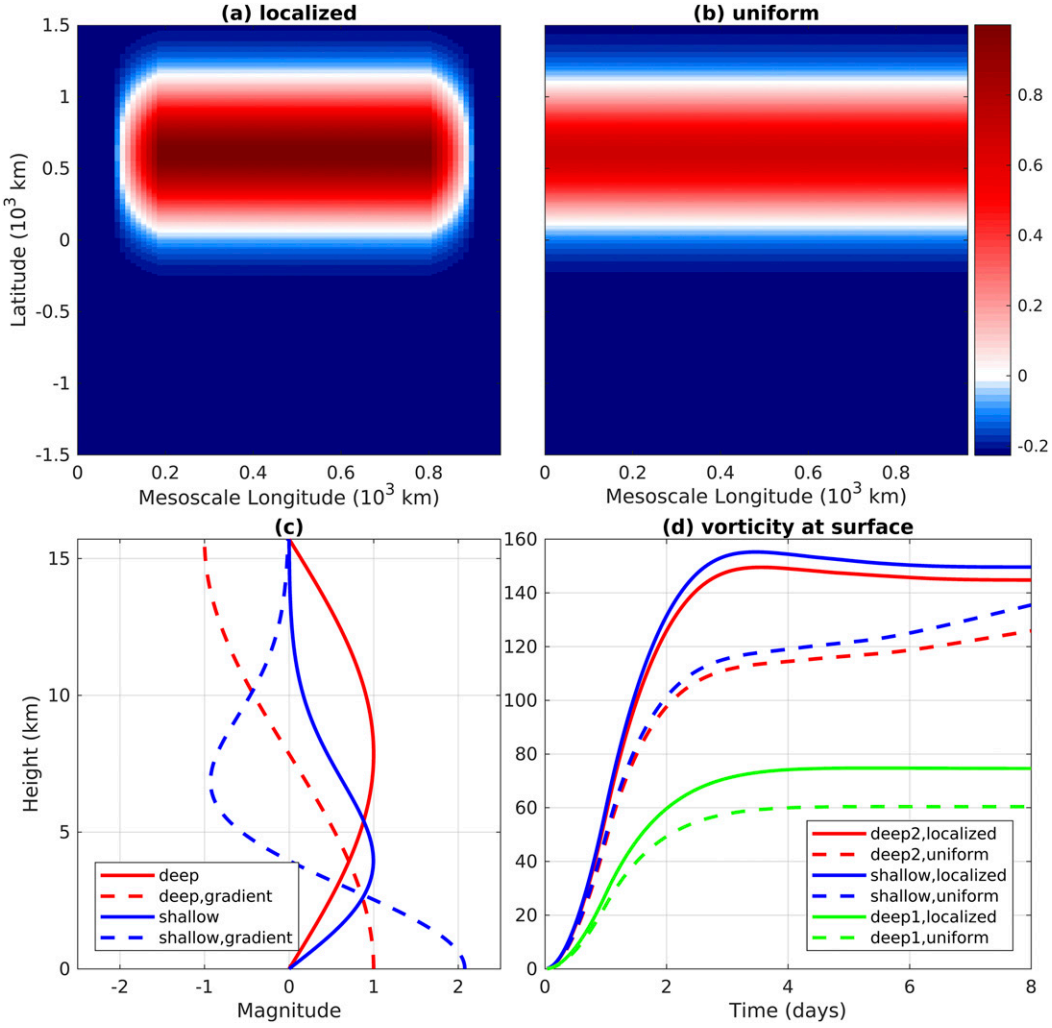

FIG. 1. Horizontal and vertical properties of heating profiles in all scenarios. (a) Horizontal profile of zonally localized heating. (b) Horizontal profile of zonally uniform heating. (c) Vertical profiles of heating and its gradient. (d) Time series of the vorticity at the surface in the Frobenius norm. The value is in dimensionless units.

is 1 (maximum heating rate 33 K day^{-1}). The horizontal profile $H(x, y)$ and time series $\phi(t)$ are the same as Eq. (16). The vertical profile of shallow congestus heating $G(z)$ is prescribed in Fig. 1c and reaches its maximum value around the height $z = 4$ km, while that of deep convective heating reaches maximum value at the height $z = 7.8$ km. Since horizontal wind divergence is proportional to the gradient of $G(z)$, the magnitude of wind convergence at the surface in the shallow congestus heating case is more than twice as much as that in the deep convective heating case, as shown in Fig. 1c. Besides, compared with the deep convective heating case, the maximum wind divergence in the shallow heating case is near the height z = 6 km, which qualitatively matches well with the returning flows above the ABL in the shallow meridional circulation (Zhang et al. 2004).

In the following discussion, two deep heating cases are considered. The strong deep heating case (deep2: magnitude coefficient $c = 2$) indicates the significant baroclinic aspects of ITCZ breakdown. The relatively weak deep heating case (deep1: magnitude coefficient $c = 1$) in the same maximum heating magnitude as the shallow heating is used for comparison with the shallow heating case. According to Fig. 1d, the spinup time for all the scenarios is around 3 days; here, the numerical solutions at day 4 are mainly chosen for discussion.

b. *Formation and undulation of a positive vorticity strip*

In the ITCZ, meridional shear of zonal winds is characterized by a positive vorticity strip in the Northern Hemisphere. Therefore, the ITCZ breakdown can

be visualized through the vorticity strip dynamics from its formation and undulation in the early stage to its breakdown into several vortices later.

Figures 2a–c show the horizontal profile of velocity and vorticity fields at the surface during the first 4 days in the deep2 heating case. At day 1 in Fig. 2a when the magnitude of diabatic heating reaches its maximum, a positive low-level vorticity strip develops on the poleward side of the diabatic heating region. At the lower latitudes of the Northern Hemisphere, southerly winds deflect to the right side because of the Coriolis force and generate westerly wind anomalies. Besides, winds in the Southern Hemisphere blow from the southeast, which has similar wind direction and magnitude as the trade winds (Wyrtki and Meyers 1976). At day 2 in Fig. 2b, the magnitude of the positive vorticity strip in the Northern Hemisphere gets strengthened. The zonally elongated vorticity strip starts to undulate, with its eastern end moving northward and western end moving southward, which is reminiscent of the undulation process of cloudiness during the ITCZ breakdown. At day 4 in Fig. 2c, the magnitude of the positive vorticity strip continuously increases and its maximum value reaches about $16\,\mathrm{day}^{-1} \approx 1.85 \times 10^{-4}\,\mathrm{s}^{-1}$, which is comparable with the observational data as well as numerical simulations (Ferreira and Schubert 1997). As both ends of the positive vorticity strip undulate in weak magnitude, a strong positive vortex forms in the middle, resembling the formation of tropical cyclones. Interestingly, the zonally elongated positive vorticity strip is always located on the northern side of the diabatic heating region, which can be explained by the first term, $Q\partial S_\theta/\partial z$, on the right-hand side of the PV equation in Eq. (12). Since the initial PV, $Q = y$, increases as the latitude goes poleward, this forcing term tends to reach its maximum magnitude in the northern side of the diabatic heating region and induce poleward displacement of positive vorticity anomalies.

The vertical structure of the deep heating in Fig. 1c reaches maximum value in the middle troposphere at height $z = 7.48\,\mathrm{km}$. Figures 2e–g show the horizontal profile of velocity and vorticity field in the middle troposphere during the first 4 days in the deep2 heating case. A positive vorticity strip is generated in the northern side of the diabatic heating region, gets strengthened at day 2 in Fig. 2f, undulates, and breaks down into a strong vortex in the middle at day 4 in Fig. 2g. Besides, a pair of vortex dipoles forms at low latitudes of the Northern Hemisphere with negative (positive) vorticity anomalies to the east (west). Such vortex dipoles can be explained through the PV equation in Eq. (12), where PV anomalies are forced by the vorticity tilting term, $-(\partial v/\partial z)(\partial S_\theta/\partial x)$. As far as the velocity field is concerned, the strong positive vortex in the northern side of the diabatic heating and the western vortex dipole come along with cyclonic flows, while the eastern vortex dipole comes along with anticyclonic flows.

Horizontal flows at the top diverge over the deep heating region and move northward and southward afterward. Figures 2i–k show the horizontal profile of velocity and vorticity fields near the top of the troposphere during the first 4 days in the deep2 heating case. As a counterpart of the positive vorticity strip at surface, a negative vorticity strip is generated in the Northern Hemisphere. Since PV is advected by the three-dimensional flow in Eq. (12), this negative vorticity strip has broader meridional extent and weaker magnitude because of the advection effects of meridionally divergent winds. Since the momentum damping strength at the top of the domain is only one-tenth of that at surface, the maximum wind magnitude at the top is much stronger than those at lower levels.

Compared with the deep convective heating in Fig. 1c, shallow congestus heating has a stronger vertical gradient near the surface when their maximum heating magnitudes are the same. Such large vertical gradient of upward motion also means stronger horizontal wind convergence at the surface, which can accelerate the ITCZ breakdown as shown in the other study (Wang and Magnusdottir 2005). Figures 3a–c show the horizontal profile of velocity and vorticity fields at the surface in the first 4 days in the shallow heating case. The velocity and vorticity fields share many similar features with those in the deep convective heating case in Figs. 2a–c, including the formation and undulation of a positive vorticity strip. In spite of the similarity, a direct comparison is not appropriate since the maximum shallow congestus heating is $33\,\mathrm{K\ day}^{-1}$, while the maximum deep convective heating is $66\,\mathrm{K\ day}^{-1}$. Figures 3d–f show the horizontal profile of velocity and vorticity fields at the surface in the deep1 heating case with a maximum heating magnitude of $33\,\mathrm{K\ day}^{-1}$. In contrast, there are no significant positive vorticity anomalies in the middle of the positive strip after 4 days. As for the horizontal wind field, both cases with deep and shallow heating share similar spatial patterns with cyclonic flows in the Northern Hemisphere, southerly winds around the equator, and southeasterly winds in the whole Southern Hemisphere, but the maximum wind strength in the deep1 heating case in Figs. 3d–f is about half that in the shallow heating case in Figs. 3a–c. In fact, such stronger horizontal velocity and vorticity fields in the shallow heating case have been emphasized in a model for hot towers in the hurricane embryo (Majda et al. 2008) and the ITCZ breakdown in three-dimensional flows (Wang and Magnusdottir 2005). Figures 3g–i

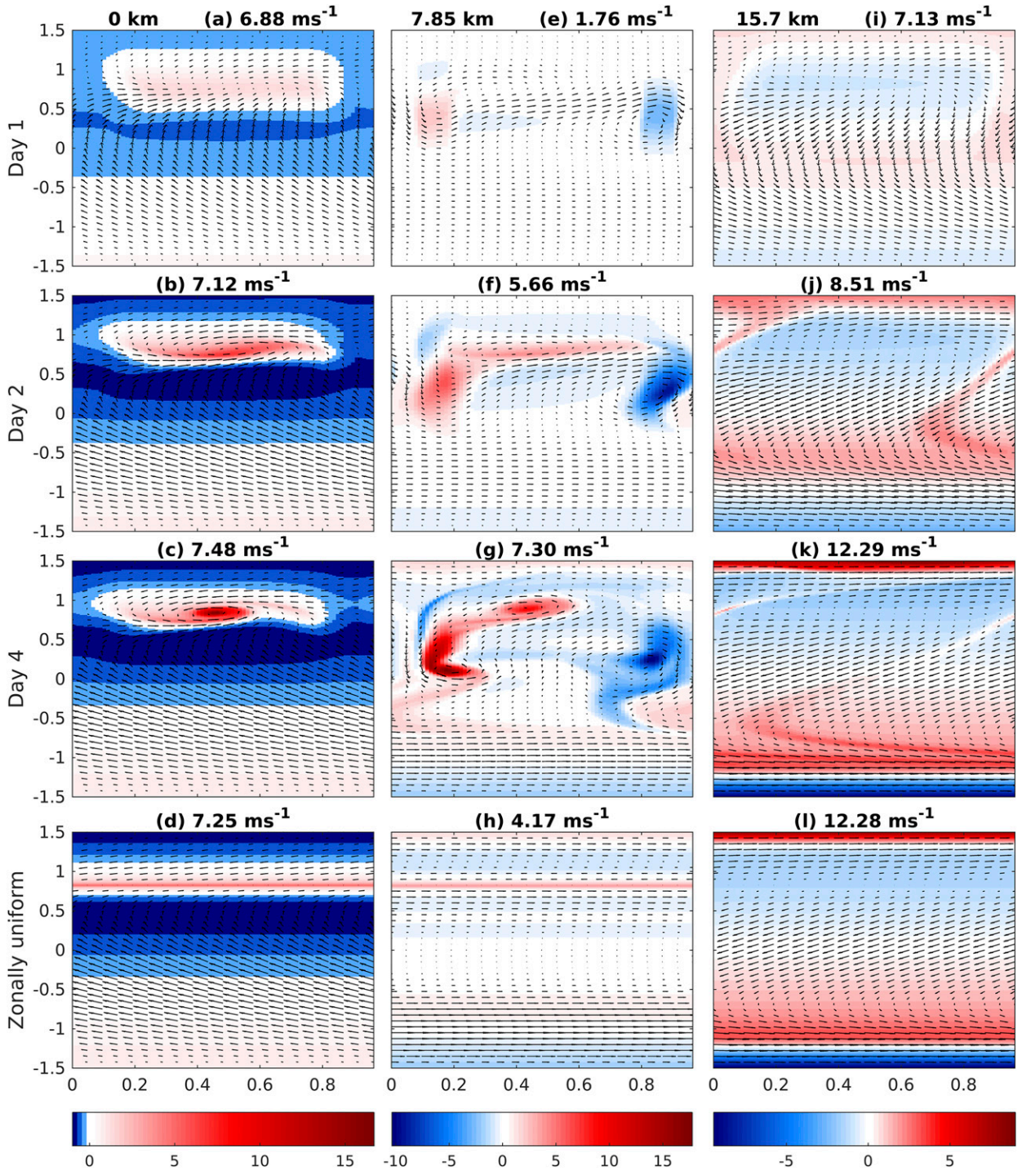

FIG. 2. Horizontal profiles of velocity (arrow) and vorticity $\omega = v_x - u_y$ (color; day^{-1}) in the mesoscale longitude (horizontal axis; 10^3 km) and latitude (vertical axis; 10^3 km) diagram in the deep2 heating case. Heights are (a)–(d) 0, (f)–(g) 7.85, and (i)–(l) 15.7 km for days (a),(e),(i) 1, (b),(f),(j) 2, and (c),(g),(k) 4. (d),(h),(l) The zonally uniform heating case at day 4. The panels in each column share the same color bar at the bottom. The maximum velocity magnitude is shown in the title of each panel.

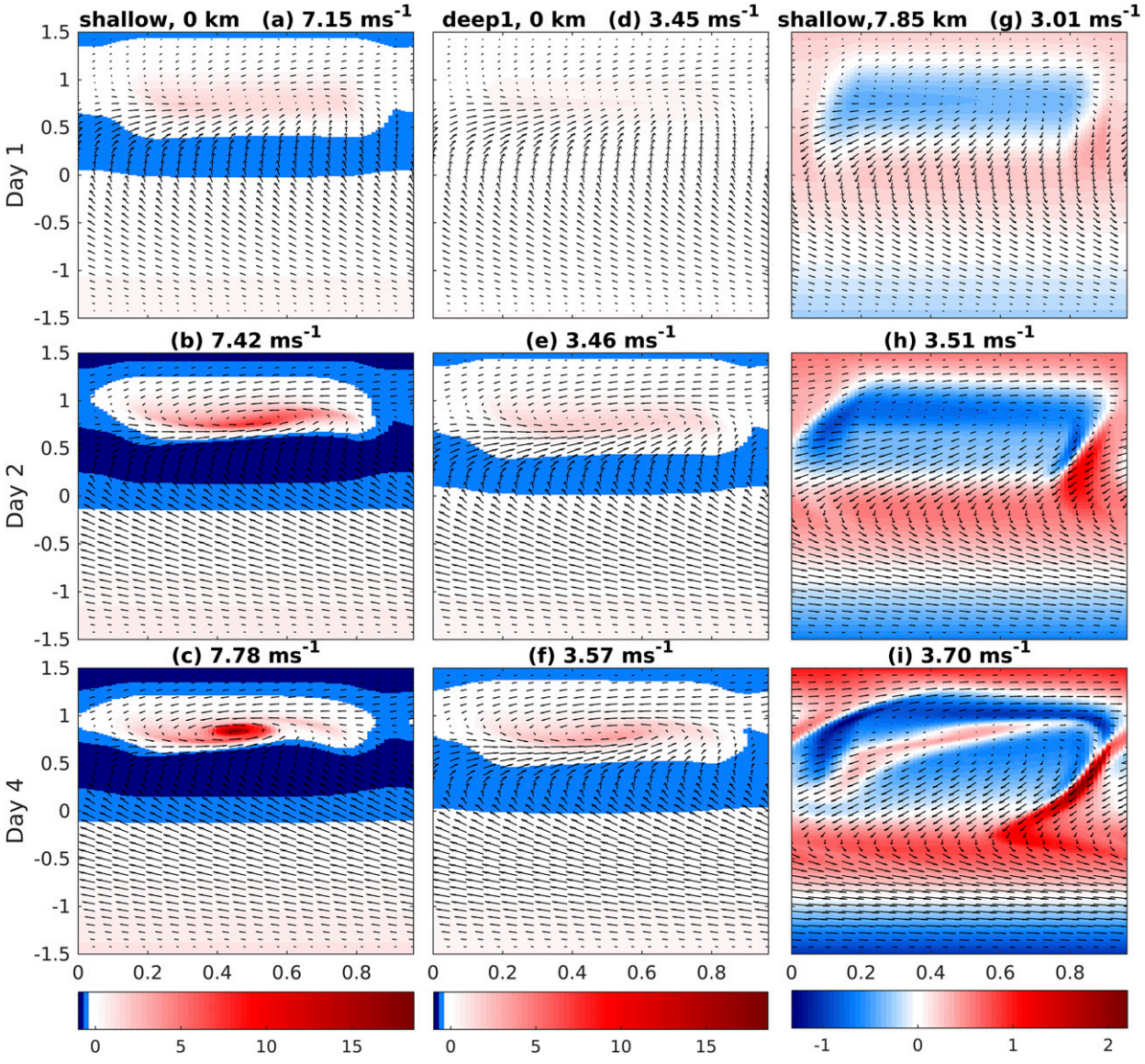

FIG. 3. As in Fig. 2, but for the shallow heating case at (a)–(c) 0 and (g)–(i) 7.85 km and (d)–(f) the deep1 heating case at 0 km for days (a),(d),(g) 1, (b),(e),(h) 2, and (c),(f),(i) 4.

show the horizontal profile of velocity and vorticity field at height $z = 7.48$ km in the shallow heating case. Again, the overall spatial pattern of the velocity and vorticity fields is quite similar to that in the deep convective heating case with doubled magnitude in Figs. 2i–k.

c. *Vertical stretching of wind and vorticity fields*

Deep clouds such as cumulonimbus have vertical extent throughout the whole troposphere; they warm and dry the entire troposphere, contributing the majority of tropical rainfall (Khouider and Majda 2008). During convective periods associated with deep clouds in the ITCZ, warm and moist air parcels have enough buoyancy to get lifted up from the ABL to the upper troposphere. Besides, the upward motion in the ITCZ has significant wind strength in the free troposphere, and it serves to transport energy and moisture from the lower troposphere to the upper troposphere. On the other hand, the MEWTG equations are fully nonlinear with the thee-dimensional advection effects. Considering that vertical velocity is directly balanced by diabatic heating in Eq. (7c), persistent upward motion exists in the diabatic heating regions, advecting both horizontal velocity and vorticity fields upward and resulting in the vertical stretching of these fields.

Figures 4a–c show the vertical profile of horizontal velocity and vorticity fields along the latitude $y = 0.8 \times 10^3$ km at day 4 in the deep2 heating case. As shown in Fig. 4c, a positive vorticity disturbance is located in the middle longitudes of the mesoscale domain with its maximum magnitude at the surface. Because of persistent upward motion in the diabatic heating region, the positive vorticity, which characterizes cyclonic flows following the ITCZ breakdown, extends to the upper troposphere. As far as the horizontal flow field in Figs. 4a and 4b is concerned, the cyclonic flows associated with the positive vortex also stretch vertically over the whole troposphere and their vertical structure becomes dominated by the barotropic mode. Figures 4d–f show the same fields in the shallow heating case.

Along with the vertical stretching of positive vorticity anomalies, winds diverge in the upper levels and go along the upper branches of the overturning circulation cells. Figures 4g–i show the vertical profile of horizontal velocity and vorticity field along the longitude $x = 0.43 \times 10^3$ km at day 4 in the deep2 heating case. As indicated by Fig. 4i, positive vorticity anomalies have very narrow meridional extent but deep vertical extent, which is accompanied by horizontal cyclonic flows, including westerly winds to the south of the positive vortex and easterly winds to the north as shown in Fig. 4g. A strong circulation cell forms around the equator, and a weak one forms at subtropical latitudes of the Northern Hemisphere, whose upper and lower branches of meridional winds are shown in Fig. 4h. Figures 4j–l show the same fields in the shallow heating case. The overall spatial pattern of velocity and vorticity fields is similar to those in the deep convective heating case except that the vertical extent is much shallower.

d. *Eddy flux divergence of zonal momentum and mean flow acceleration–deceleration*

In the M-ITCZ equations, eddy flux divergence of zonal momentum arising from the mesoscale dynamics forces the planetary-scale circulation, while the large-scale flow field provides the background mean flow for the mesoscale dynamics. Specifically, the planetary-scale zonal momentum equation reads as Eq. (11a) but without the term $-\partial\Pi/\partial X$, which vanishes in this zonally symmetric planetary-scale flow scenario. In fact, the eddy flux divergence of zonal momentum,

$$F^U = -\frac{\partial}{\partial y}(\overline{v'u'}) - \frac{\partial}{\partial z}(\overline{w'u'}), \tag{17}$$

is referred to as the convective momentum transport (CMT) and has been studied from different perspectives to highlight its significance, such as stochastic models (Majda and Stechmann 2008; Khouider et al. 2012) and dynamical models with cloud parameterization (Majda and Stechmann 2009).

The eddy flux divergence of zonal momentum F^U in Eq. (17) constitutes an upscale zonal momentum forcing on the planetary scale that can have a significant impact on the planetary-scale flow. Specifically, positive (negative) anomalies of F^U represent eastward (westward) momentum forcing. Figures 5a–c show F^U in the latitude–height diagram at day 4 in the deep2 heating case. Along the latitude where the positive vortex is located (see Fig. 4i), eastward momentum forcing is induced by F^U with deep vertical extent, which is mainly contributed by meridional transport of eddy zonal momentum $-(\partial/\partial y)(\overline{v'u'})$ in Fig. 5b. In addition, meridionally alternating eastward and westward momentum forcing exists at low latitudes and the middle troposphere of the Northern Hemisphere in Fig. 5a, which is directly related to the vorticity dipoles as shown in Fig. 2g. Figures 5d–f show the same fields in the shallow heating case. The most significant F^U anomalies are similar to those in the deep2 heating case but confined in the lower troposphere. To compare the eddy flux divergence of zonal momentum, Figs. 5g–i show the same fields in the deep1 heating case. The magnitudes of total eddy flux divergence of zonal momentum and both meridional and vertical transport of eddy zonal momentum are much weaker than those in the shallow heating case in Figs. 5d–f, highlighting the significant upscale impact in the shallow heating case.

The impact of F^U can be illustrated through the comparison between numerical solutions with and without the eddy momentum forcing F^U. Instead of utilizing the mesoscale zonally localized diabatic heating in Fig. 1a, a mesoscale zonally uniform heating profile is prescribed in the same expression in Eq. (16), but its horizontal envelope function $H(y)$ is replaced by the one in Fig. 1b with the same zonal mean. The differences of mesoscale zonal mean of zonal velocity reflect the impact of eddy flux divergence of zonal momentum on the planetary-scale circulation. Figures 6a and 6b show mean zonal velocity $\overline{u}$ in the latitude–height diagram at day 4 in the zonally localized and uniform deep2 heating case. In particular, the horizontal profiles of velocity and vorticity fields at different levels in the zonally uniform heating case are shown in Figs. 2d, 2h, and 2l. In Fig. 6c, there are westerly wind anomalies along the latitude of the positive vortex (see Fig. 4i), which matches well with the eastward momentum forcing in the same region in Fig. 5a. Because of the advection effect of the mean meridional circulation $(\overline{v}, \overline{w})$, such eastward zonal wind anomalies extend to the upper troposphere, the equator, and the Southern Hemisphere. Besides, there are meridionally opposite-signed zonal wind anomalies

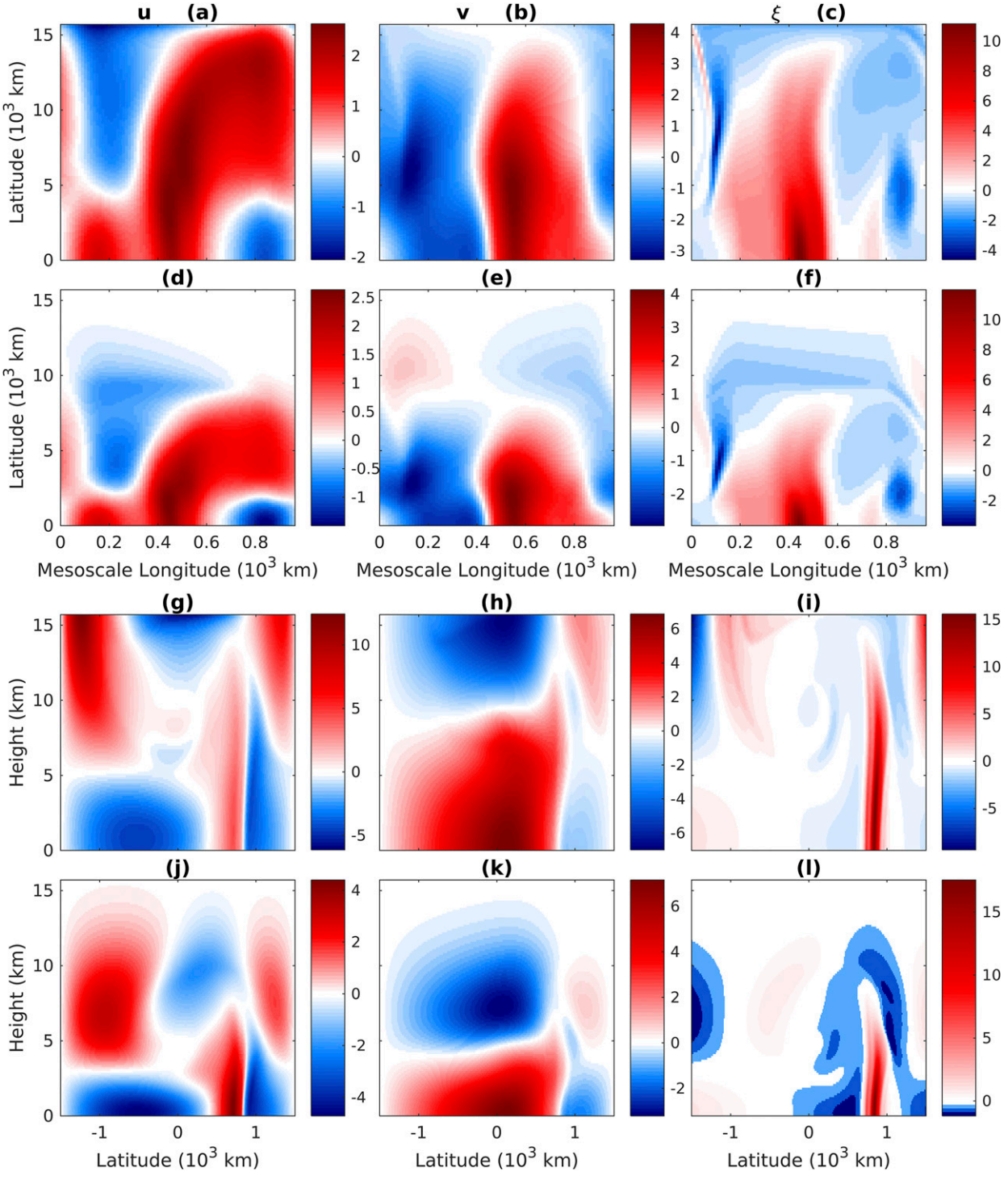

FIG. 4. Vertical profiles of (a),(d),(g),(j) zonal velocity, (b),(e),(h),(k) meridional velocity, and (c),(f),(i),(l) vorticity at day 4. (a)–(c) Solutions along the latitude 0.8×10^3 km in the deep2 heating case. (g)–(i) Solutions along the longitude 0.43×10^3 km in the deep2 heating case. (d)–(f),(j)–(l) As in (a)–(c) and (g)–(i), respectively, but for the shallow heating case. The dimensional units of horizontal velocity and vorticity are m s^{-1} and day^{-1}, respectively.

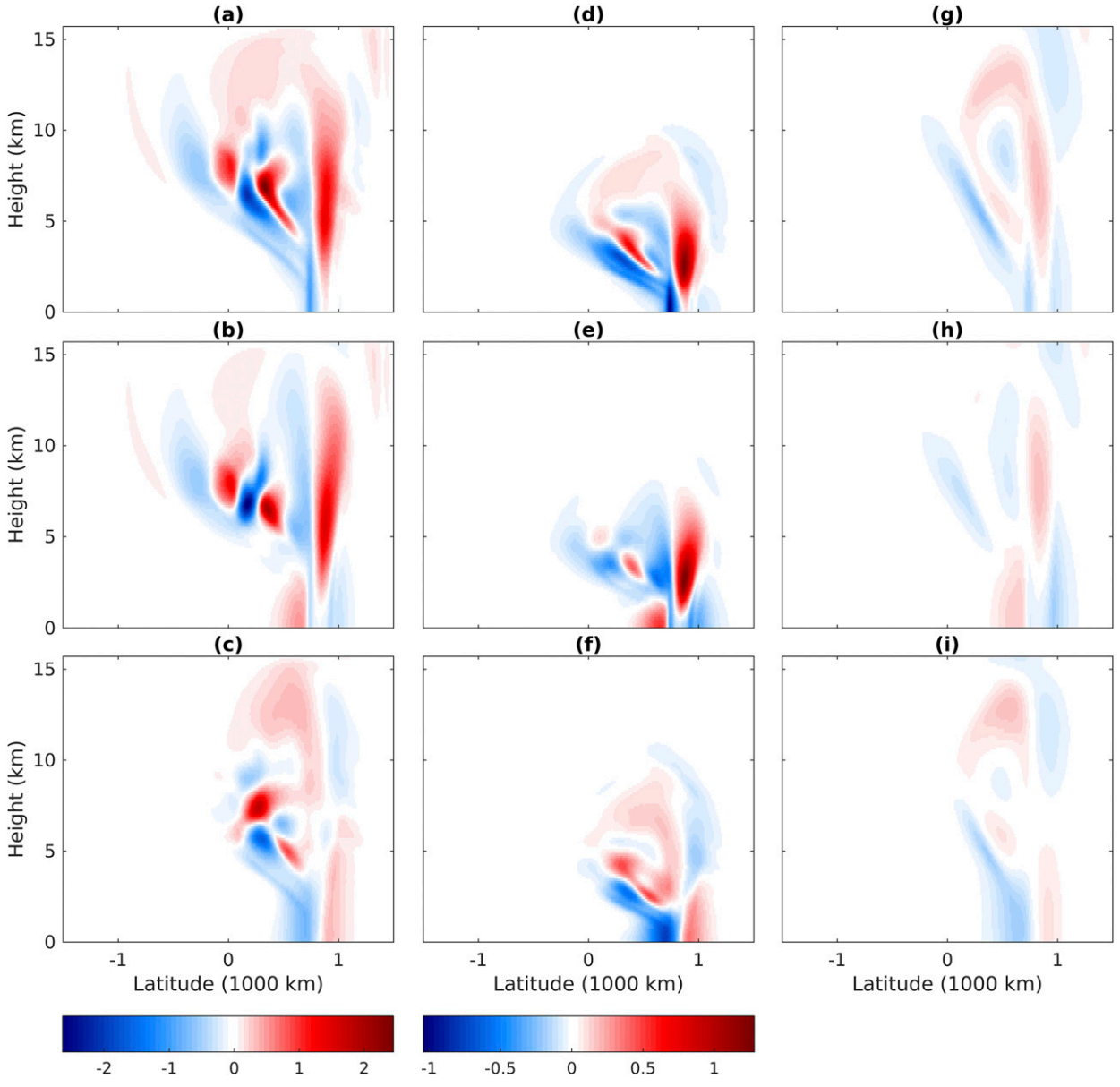

FIG. 5. Eddy flux divergence of zonal momentum F^U ($\mathrm{m\,s^{-1}\,day^{-1}}$) in the latitude–height diagram at day 4 for the (a)–(c) deep2, (d)–(f) shallow, and (g)–(i) deep1 heating cases [(d)–(f) share the same color bar at the bottom with (g)–(i)]. (a) F^U, (b) $-(\partial/\partial y)(\overline{v'u'})$, and (c) $-(\partial/\partial z)(\overline{w'u'})$.

in the middle troposphere and low latitudes of the Northern Hemisphere. Figures 6d–f show the same fields in the shallow heating case. The overall spatial patterns of mean zonal velocity and zonal velocity anomalies are mostly confined in the shallower levels.

The eddy flux divergence of zonal momentum in Eq. (17) is a crucial quantity, because it not only significantly modifies the zonal momentum budget as momentum forcing but also involves energy transfer across multiple spatial scales and induces acceleration–deceleration effects on the planetary-scale mean flow. In fact, several studies based on reanalysis datasets have been undertaken to estimate atmospheric momentum, energy, and heat budgets and discuss how Hadley cells get influenced by eddy transports (Trenberth and Stepaniak 2003a,b; Schneider 2006; Schneider et al. 2010). Here, the acceleration and deceleration of eddy flux divergence of zonal momentum is investigated through the kinetic energy of zonal winds instead of the total kinetic energy in Eq. (14). One essential reason is that only the mesoscale mean zonal velocity is

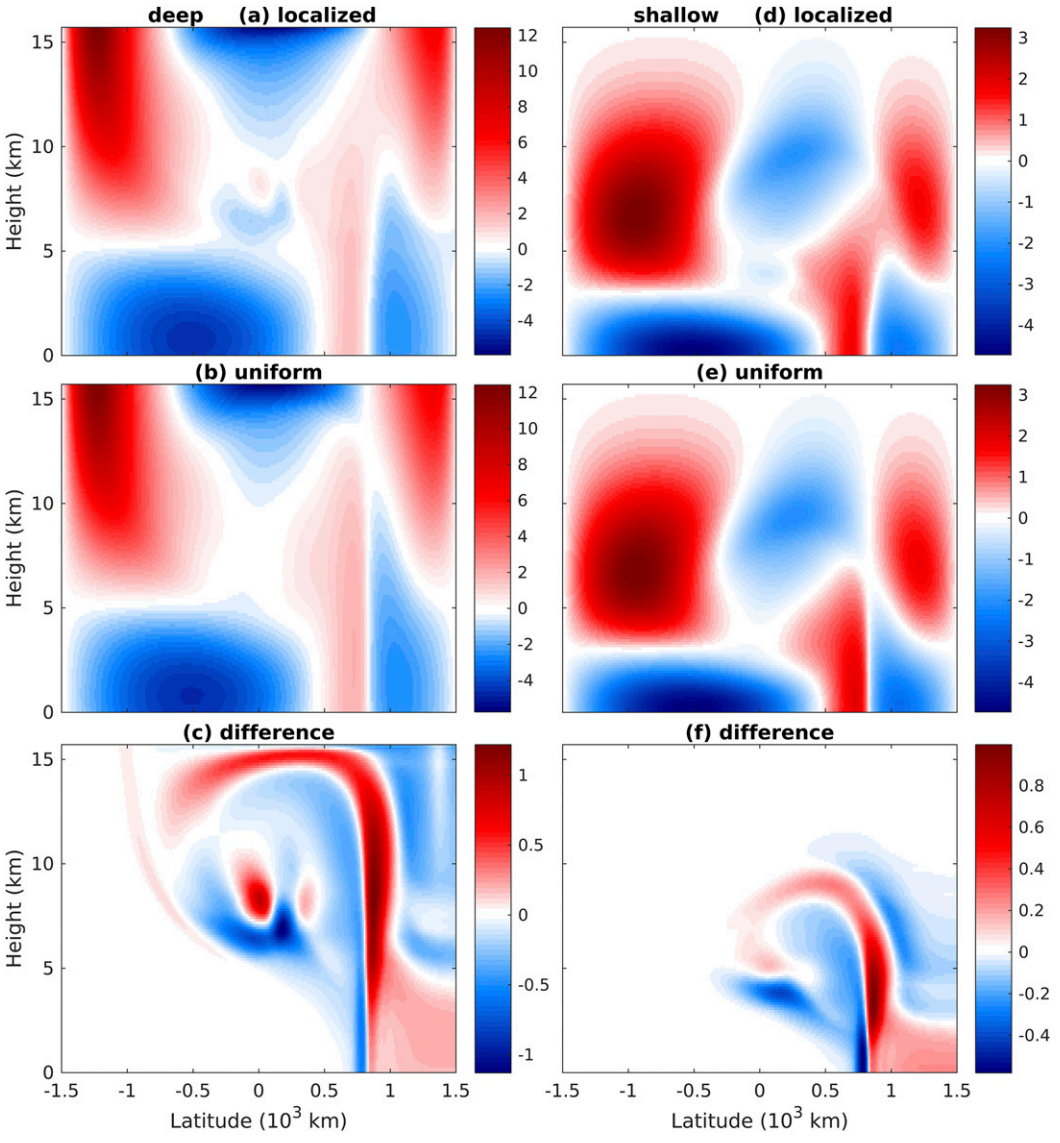

FIG. 6. Mean zonal velocity $\overline{u}$ (m s^{-1}) in the latitude–height diagram at day 4. Solutions for (a) zonally localized heating, (b) zonally uniform heating, and (c) their difference in the deep2 heating case. (d)–(f) As in (a)–(c), respectively, but for the shallow heating case.

coupled with the planetary-scale gravity waves in Eqs. (11a) and (7e)–(7g), while the mean meridional velocity is directly balanced by the diabatic heating through Eqs. (11b) and (11c). The equation for kinetic energy of mean zonal velocity is reduced from Eq. (14),

$$\frac{\partial K^u}{\partial t} + \frac{\partial}{\partial y}(\overline{v}K^u) + \frac{\partial}{\partial z}(\overline{w}K^u) = y\overline{v}\,\overline{u} - 2dK^u + F^u\overline{u}, \qquad (18)$$

where $K^u = \overline{u}^2/2$ represents kinetic energy of planetary-scale zonal winds, and the eddy energy transfer term $F^u\overline{u}$ can be interpreted as the acceleration–deceleration effects of F^u on the mean zonal winds.

Figure 7a shows acceleration–deceleration effects of eddy flux divergence of zonal momentum at day 4 in the deep2 heating case. Along the latitude where the positive vortex is located (see Fig. 4i), the acceleration effects are induced by eastward momentum forcing F^u on the westerly mean flows $\overline{u}$. To both the northern and southern sides of those acceleration effects, the deceleration effects with narrow meridional extent are mostly significant in the lower troposphere, which decelerate the westerly (easterly) winds to the south (north) of the positive vortex. At low latitudes of the Northern Hemisphere, acceleration effects are also significant in the middle troposphere where mean zonal winds are weak in Fig. 6b

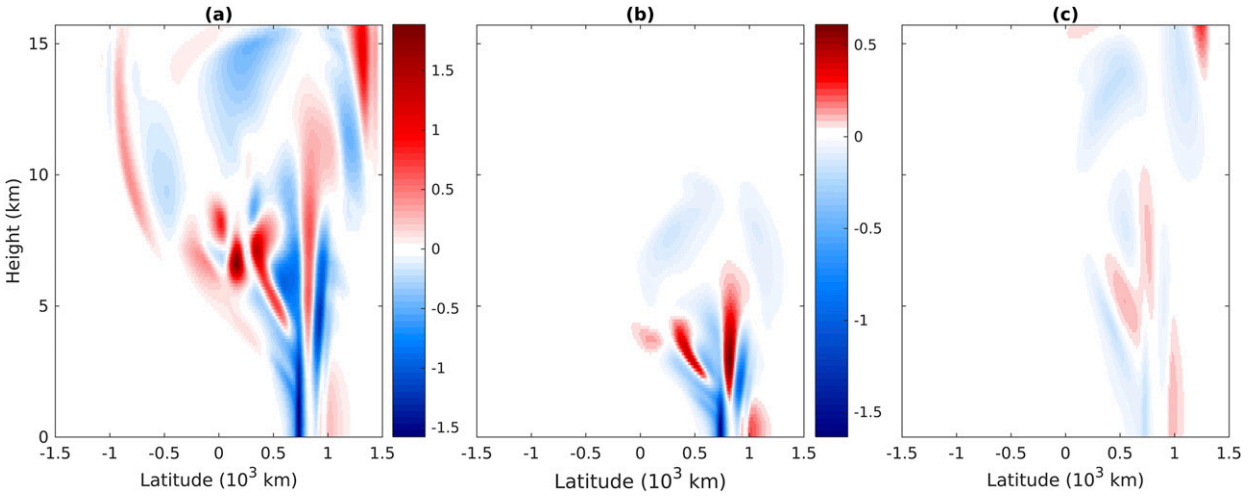

FIG. 7. Acceleration and deceleration of mean zonal velocity ($m^2\,s^{-2}\,day^{-1}$) due to eddy flux divergence of zonal momentum in the latitude–height diagram at day 4. The color indicates the value of $F^U\overline{u}$ with positive anomalies for acceleration effects and negative anomalies for deceleration effects for the (a) deep2, (b) shallow, and (c) deep1 cases.

and modified mainly by eddy flux divergence of zonal momentum in Fig. 5a. Figure 7b shows the acceleration–deceleration effects due to eddy flux divergence of zonal momentum in the shallow heating case. The most significant acceleration–deceleration effects are confined in the lower troposphere. As a clear comparison, the eddy energy transfer $F^u\overline{u}$ in the deep1 heating case in Fig. 7c is much weaker than that in the shallow heating case in Fig. 7b, highlighting the significant upscale impact of mesoscale fluctuations in the shallow congestus heating in terms of kinetic energy budget.

4. ITCZ breakdown in zonally varying planetary-scale flow

In this section, the M-ITCZ equations are utilized to simulate the ITCZ breakdown process over the EP involving both the mesoscale and planetary-scale dynamics. In each mesoscale cell, periodic boundary conditions are imposed in the zonal direction and rigid-lid boundary conditions are imposed in the meridional and vertical directions. On the planetary scale, the zonal periodic boundary condition is naturally consistent with the belt of tropics around the globe. The model is driven by diabatic heating on both mesoscale and planetary scale, and all physical variables are initialized from a background state of rest. The whole domain is discretized with nested coarse and fine grids as shown in Fig. 8. All the other model setup and numerical details such as mesoscale and planetary-scale domain size and spatial and temporal resolutions are summarized in the appendix.

To model the ITCZ over the EP, diabatic heating S_θ is modulated by a planetary-scale zonally localized envelope. In general, such a two-scale diabatic heating S_θ in dimensionless units reads as follows:

$$S_\theta = cF(X)H(x,y)G(z)\phi(t), \tag{19}$$

where $F(X) = 1.2e^{-(X-4)^2}$ is the planetary-scale envelope function; $H(x, y)$ is the horizontal heating profile, which can be either mesoscale zonally localized heating in Fig. 1a or uniform heating in Fig. 1b; and $G(z)$ is the vertical heating profile, which can have either deep or shallow vertical extent in Fig. 1c. The magnitude parameter c and the time series $\phi(t)$ are as in section 3.

a. *Cross section of mean zonal velocity in the heating region*

Here, two numerical simulations are implemented for comparison, both of which are driven by deep2 heating modulated by a large-scale envelope. The only difference between these two simulations is that the heating in one case varies on the mesoscale and that in the other case is zonally uniform on the mesoscale, similar to those in Figs. 6a–c. Then the difference of zonal velocity between these two simulations indicates the impact of eddy flux divergence of zonal momentum on the planetary-scale circulation. Figure 9a shows the cross section of planetary-scale zonal velocity anomalies in the center of the heating region at day 4 in the deep2 heating case. The overall spatial pattern of zonal velocity anomalies here is quite similar to that in the planetary-scale zonal symmetric case in Fig. 6c, including westerly wind anomalies in deep vertical extent near the latitude $y = 800$ km with its maximum strength in the middle troposphere and opposite-signed mean zonal velocity anomalies in the

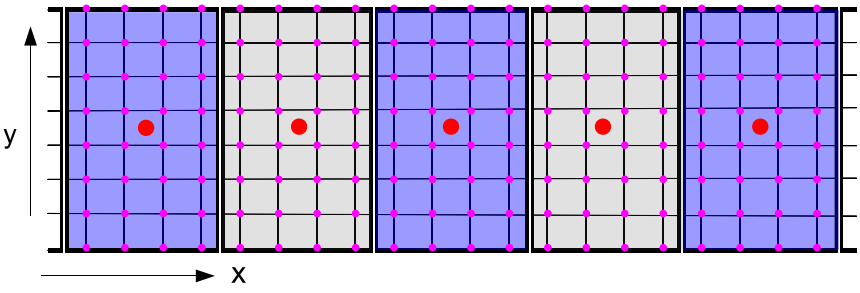

FIG. 8. A schematic depiction of the multiscale domain with nested grids. The large red dots are the coarse grid points on the planetary scale. Each coarse grid point corresponds to a single mesoscale domain characterized by a mesoscale box in thick lines. The fine grid points in each mesoscale domain are shown by pink dots. In the actual simulations, there is a total of 41 coarse grid points, namely, 41 mesoscale domains. Within each mesoscale domain, there are 241 × 81 horizontal fine grid points and 127 vertical grid points. More details can be found in Table 1.

middle troposphere near the equator. In contrast, Fig. 9b shows the cross section of planetary-scale zonal velocity anomalies in the shallow heating case. Compared with the deep convective heating case in Fig. 9a, the zonal velocity anomalies on the planetary scale are mostly confined in the lower troposphere, which is consistent with the limited vertical extent of the shallow congestus heating. Meanwhile, the spatial pattern of zonal velocity anomalies is quite similar to the planetary-scale zonally symmetric case in Fig. 6f.

b. *Mean zonal velocity in the lower, middle, and upper troposphere*

Figures 10a–c show planetary-scale zonal velocity anomalies at three different levels at day 4 in the deep2 heating case. The significant zonal velocity anomalies are confined in the longitudes between $X = 15 \times 10^3$ and 25×10^3 km, which is the same as the zonal extent of the convective envelope in Eq. (19). In the lower troposphere in Fig. 10c, westerly wind anomalies are localized in the northern side of the diabatic heating and weak easterly wind anomalies are to the south. In the middle troposphere in Fig. 10b, the westerly wind anomalies at subtropical latitudes of the Northern Hemisphere have stronger magnitude and broader zonal extent. Besides, there are easterly wind anomalies at low latitudes of the Northern Hemisphere and westerly wind anomalies to their south and north. The zonal velocity anomalies in the upper troposphere in Fig. 10a are dominated by westerly winds with broad meridional extent, including low latitudes of both the Northern and Southern Hemispheres as well as the equator. In contrast, planetary-scale zonal velocity anomalies at these three levels at day 4 in the shallow-heating case are shown in Figs. 10d–f. At the surface in Fig. 10f, there are westerly wind anomalies at subtropical latitudes of the Northern Hemisphere and easterly wind anomalies to the south, whose spatial pattern is quite similar to the deep convective heating case in Fig. 10c. In the middle troposphere in Fig. 10e, easterly wind anomalies are found to the north of the westerly wind anomalies in the Northern Hemisphere. In the upper troposphere in Fig. 10d, the magnitude of zonal velocity anomalies is negligible.

c. *Upscale impact of mesoscale fluctuations on planetary-scale gravity waves*

In the M-ITCZ equations, the planetary-scale physical variables including large-scale zonal velocity $\langle \overline{u} \rangle$, pressure perturbation Π, potential temperature anomalies Θ, and vertical motion W do not depend on meridional coordinate y, representing a planetary-scale gravity wave with uniform meridional profile. Therefore, the meridional mean of zonal velocity and potential temperature anomalies can be used to characterize planetary-scale gravity waves.

Figure 11 shows meridionally averaged planetary-scale zonal velocity in the longitude–latitude diagram from those two simulations in section 4a. It turns out that meridionally averaged planetary-scale zonal velocity in Figs. 11a and 11b has few discrepancies in the deep2 cases with or without mesoscale fluctuations. In a nutshell, deep heating in the middle of the domain tends to drive both eastward- and westward-propagating gravity waves, bringing lower-tropospheric easterlies (upper-tropospheric westerlies away from the heating region). Figure 11c shows the difference of zonal velocity between those two simulations with or without mesoscale fluctuations, characterizing the upscale impact on planetary-scale gravity waves. It is found that planetary-scale zonal velocity anomalies in Fig. 11c have weak magnitude and narrow zonal extent. Such weak magnitude of zonal velocity anomalies is associated with

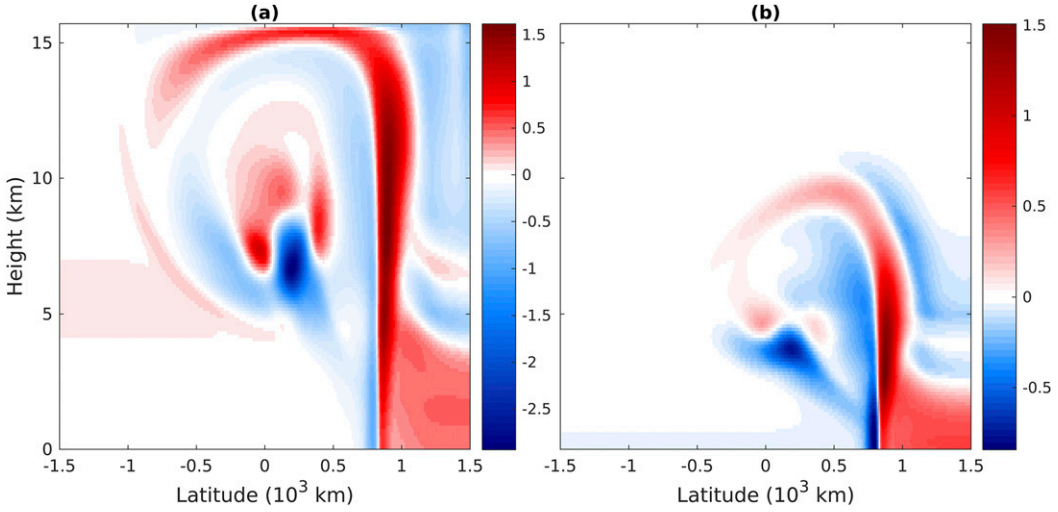

FIG. 9. Cross section of mean zonal velocity anomalies ($m\,s^{-1}$) in the center of heating region (longitude $X = 19.51 \times 10^3$ km) at day 4 for (a) the deep2 heating case and (b) the shallow heating case.

their opposite-signed meridional profile as shown in Figs. 10a–c. The narrow zonal extent of zonal velocity anomalies can be explained by the fact that they are dominated by higher baroclinic modes. In general, gravity waves in higher baroclinic modes have slower phase speeds and propagate over shorter distances under momentum damping. Since zonal velocity driven by mean heating in Fig. 11e is dominated by the first baroclinic mode, significant zonal velocity in the first baroclinic mode is carried away from the heating region by planetary-scale gravity waves at the phase speed of $50\,m\,s^{-1}$, while that in higher baroclinic modes are mostly confined in the heating region. After 4 days since initialization, planetary-scale gravity waves in the first baroclinic modes propagate over a distance as far as 1.7×10^4 km with their magnitudes only damped by half by cumulus drag (averaged dissipation time of 5 days). In contrast, as shown by Fig. 11f, planetary-scale zonal velocity anomalies induced by upscale impact of mesoscale fluctuations are dominated by the second and third baroclinic modes and thus propagate over much shorter distances. A quick comparison about planetary-scale zonal velocity anomalies is undertaken between the case with localized planetary-scale flow and that with uniform planetary-scale flow. According to Fig. 11d, significant differences of planetary-scale zonal velocity anomalies exist in the middle and lower troposphere, indicating nonlocal interactions of flow fields from different mesoscale domains through planetary-scale gravity waves. To sum up, most significant upscale impact of mesoscale fluctuations is confined in the heating region, while little upscale impact is transported away by planetary-scale gravity waves, which also applies to the shallow heating case (not shown). Moreover, it is worthwhile noting that, in addition to being confined to the region of planetary-scale heating envelope, the meridionally averaged eddy flux disturbances are relatively weak (about 10% of the total planetary response). This is perhaps a limitation of the multiscale model, which does not carry a planetary-scale meridional variable.

5. Concluding discussion

Capturing the flow fields in the baroclinic modes during the ITCZ breakdown, including the undulation of a positive vorticity strip and the formation of a strong positive vortex, is one of the main motivations in this paper. Using a multiscale model to incorporate both the mesoscale and planetary-scale dynamics during the ITCZ breakdown and assessing the upscale impact of mesoscale fluctuations on the planetary-scale circulation is the other main motivation. Here, a multiscale model (M-ITCZ equations) is used to achieve those motivations as mentioned above. Specifically, the undulation of a positive vorticity strip and formation of a strong positive vortex are simulated on the mesoscale dynamics of the M-ITCZ equations, which resembles the formation of tropical cyclones during the ITCZ breakdown. The planetary-scale circulation is governed by the planetary-scale gravity wave equations in the M-ITCZ equations.

In the first scenario, the planetary-scale flow is assumed to be zonally symmetric, which suppresses planetary-scale gravity waves in the M-ITCZ equations. Deep convective heating is prescribed as the mesoscale

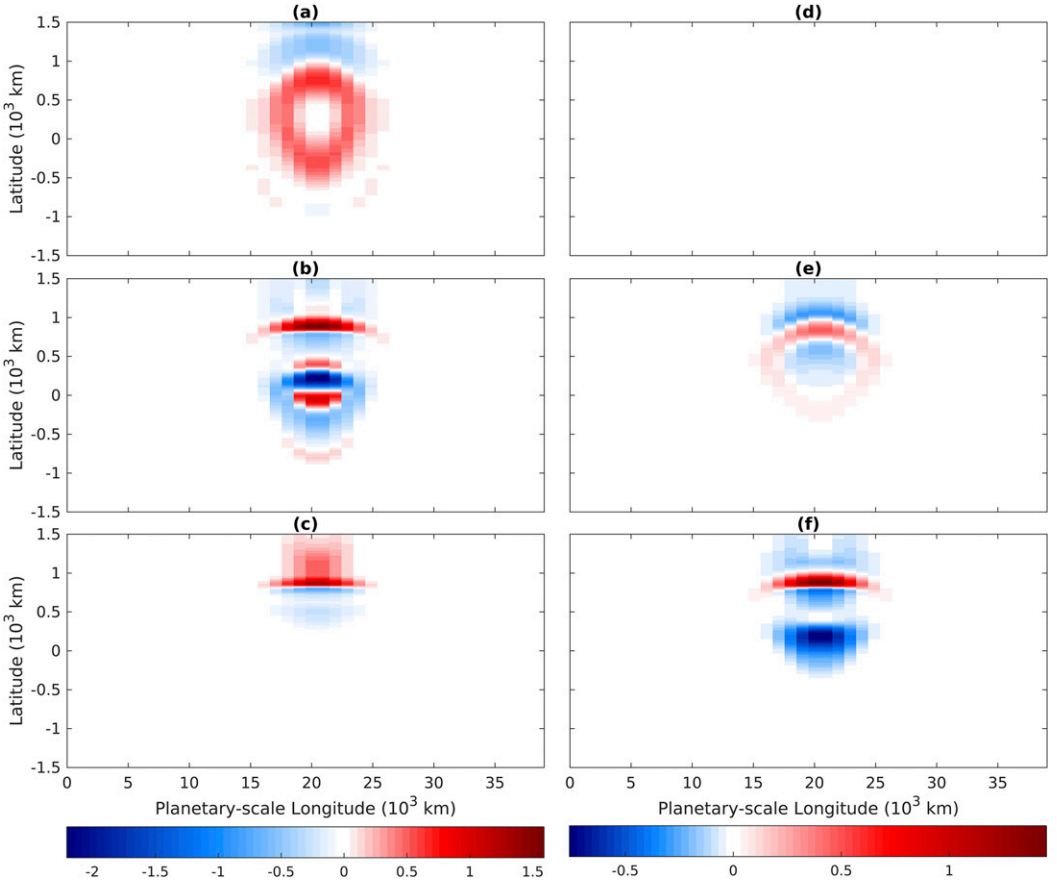

FIG. 10. Longitude–latitude diagrams of mean zonal velocity anomalies (m s^{-1}) at different heights at day 4 in the for (a)–(c) the deep2 heating case and (d)–(f) the shallow heating case for heights of (a),(d) 14.84, (b),(e) 7.48, and (c),(f) 3.62 km.

zonally localized heating in the Northern Hemisphere and uniform cooling elsewhere in the first baroclinic mode. First, after the flow field is initialized from a background state of rest, a positive vorticity strip forms at the surface in the northern side of the diabatic heating region, surrounded by negative vorticity anomalies. As the diabatic heating remains persistent, the positive vorticity strip has increasing magnitude and starts to undulate, which resembles the undulation of the ITCZ as observed in Ferreira and Schubert (1997). Later, a strong positive vortex is generated in the middle of the positive vorticity strip, which mimics tropical cyclogenesis in the baroclinic modes during the ITCZ breakdown. Since upward motion prevails in the diabatic heating region, positive vorticity anomalies are advected by upward motion and stretched vertically to the middle and upper troposphere. Second, the eddy flux divergence of zonal momentum is characterized by midlevel (low level) eastward (westward) momentum forcing with deep vertical extent at subtropical latitudes of the Northern Hemisphere and midlevel opposite-signed momentum forcing anomalies at low latitudes. Such eddy flux divergence of zonal momentum tends to induce westerly wind anomalies at subtropical latitudes of the Northern Hemisphere, which are further advected by upper-level northerly winds to the Southern Hemisphere. Besides, midlevel easterly and westerly wind anomalies are also induced at low latitudes of the Northern Hemisphere, which provide extensive features for the zonal jets in this region. Third, as far as the kinetic energy budget is concerned, acceleration effects are induced in the region where the positive vorticity anomalies are vertically stretched, while deceleration effects are mainly located in the lower troposphere to the north and south of the positive vorticity strip. Besides, strong acceleration effects are also induced in the middle troposphere at low latitudes of the Northern Hemisphere, where the wind directions and strength are changed dramatically. Such a discussion about eddy flux divergence of zonal momentum and its acceleration–deceleration effect on zonal jets should be useful to help improve convective parameterizations in global climate models (GCMs). In fact, the crucial

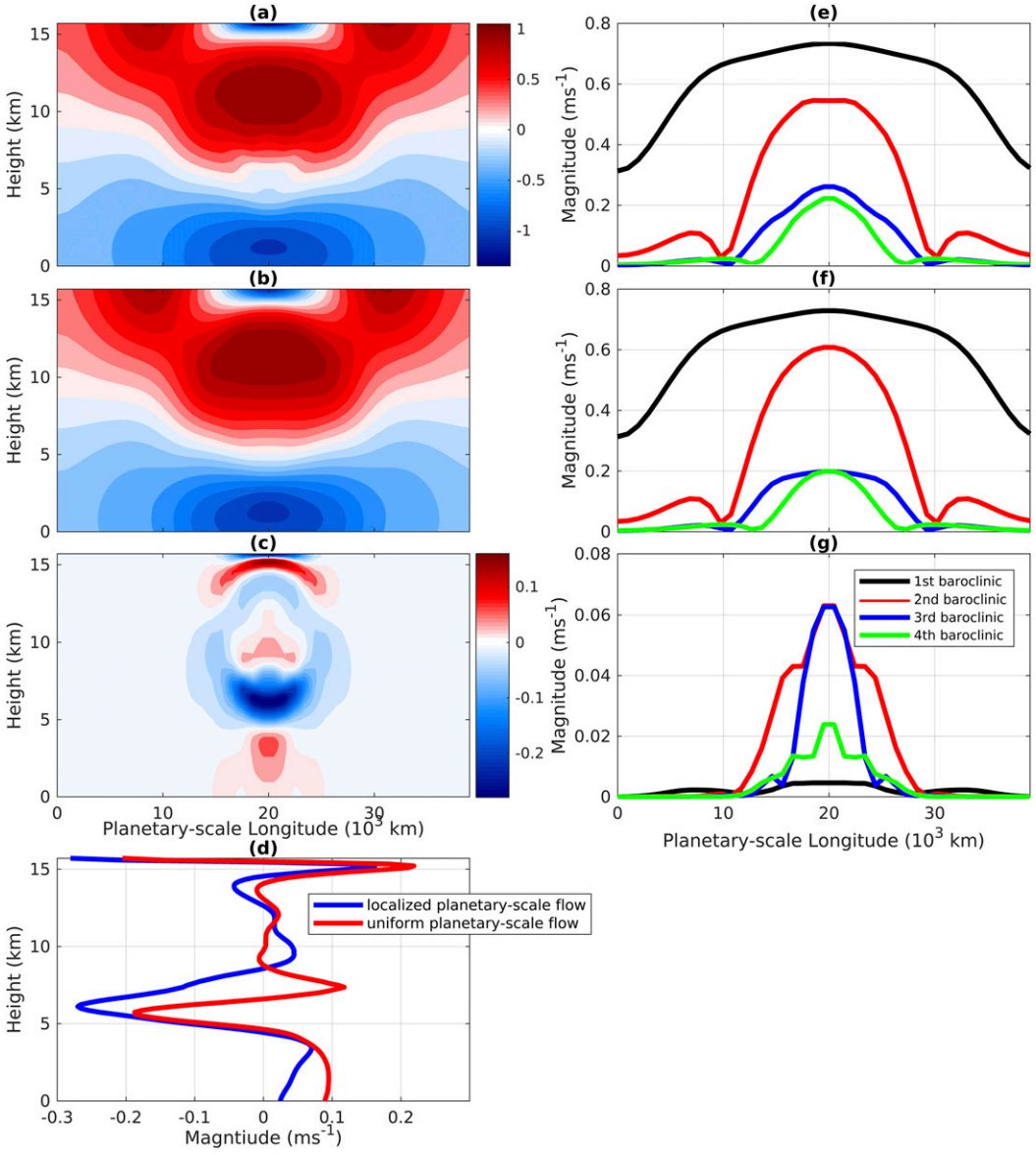

FIG. 11. Meridionally averaged planetary-scale zonal velocity (m s^{-1}) in the longitude–height diagram at day 4. (a) Zonal velocity induced by mesoscale zonally localized deep2 heating and (b) zonal velocity induced by mesoscale zonally uniform deep2 heating [(a) and (b) share the same color bar]. (c) The difference between (a) and (b). (e)–(g) Magnitudes (absolute value) of the first four baroclinic modes of zonal velocity in (a)–(c), respectively. (d) The vertical profile of planetary-scale zonal velocity anomalies at $X = 19.51 \times 10^3$ km. The blue curve corresponds to the localized planetary-scale flow case as shown in (c), while the red curve corresponds to the uniform planetary-scale flow case as discussed in section 3.

features of upscale impact of mesoscale fluctuations on the large-scale circulation and precipitation are still poorly simulated in the GCMs, which is mainly related to the fact that the resolution of GCMs is too coarse to explicitly simulate the dynamical and thermal properties of tropical flows on the mesoscale. However, several recent studies have been undertaken to take into account the upscale impact of mesoscale fluctuations in convective parameterizations (Goswami et al. 2017; Moncrieff et al. 2017), providing encouraging results for the feasibility and necessity of using the M-ITCZ model to parameterize the upscale impact of the ITCZ breakdown on the planetary-scale circulation.

Compared with deep convective heating, shallow congestus heating is prescribed in a vertical profile with its maximum in the lower troposphere. A direct

comparison between the deep and shallow heating cases with the same maximum heating magnitude indicates that shallow congestus heating induces stronger vorticity anomalies and wind strength at the surface. In fact, such stronger cyclonic flows driven by shallow congestus heating is also discussed in a canonical balanced model to simulate ''hot towers'' in the hurricane embryo (Majda et al. 2008). In the three-dimensional simulation for ITCZ breakdown of Wang and Magnusdottir (2005) using a primitive-equation model, shallow heating tends to induce stronger lower-tropospheric potential vorticity response than the deep heating, while the upper-tropospheric potential vorticity response vanishes. Shallow congestus heating also induces stronger eddy flux divergence of zonal momentum on the planetary-scale zonal winds. Third, as for the kinetic energy budget, there are stronger acceleration effects in the region where the positive vorticity anomalies are vertically stretched and deceleration effects to its north and south. Besides, acceleration effects are also stronger in the lower troposphere at low latitudes of the Northern Hemisphere. In fact, it has been recognized that shallow convection plays an important role in tropical climate dynamics (Neggers et al. 2007). Except for several encouraging attempts (Bretherton et al. 2004; Kuang and Bretherton 2006), shallow convection and the transition from shallow to deep cumulus convection are still poorly simulated in the current convective parameterization. In addition, the shallow meridional circulation is incorrectly simulated by most of GCMs (Zhang et al. 2004), which may be related with the inadequate treatment of shallow convection as well.

In the second scenario, the diabatic heating is modulated by a planetary-scale zonally localized convective envelope to mimic the EP ITCZ and the fully coupled M-ITCZ equations that allow zonal variation of flow fields on both the mesoscale and planetary scale are used. As modulated by the planetary-scale convective envelope, the flow fields in all the mesoscale domains are characterized by cyclonic flow in the same direction in the Northern Hemisphere. Through comparison between mesoscale zonally uniform and localized heating cases, significant zonal velocity anomalies are induced in the diabatic heating region, which mainly consist of deep westerly wind anomalies at subtropical latitudes of the Northern Hemisphere and several easterly or westerly wind anomalies in the middle troposphere near the equator. Last, the eddy flux divergence of zonal momentum has weak impact on the meridional mean of zonal velocity and potential temperature in both deep and shallow heating cases; thus, small upscale impact of mesoscale fluctuations are transported away from the diabatic heating region by the planetary-scale gravity waves.

This study based on a multiscale model has several implications for physical interpretation and comprehensive numerical models. The M-ITCZ equations incorporate both the ITCZ breakdown and planetary-scale circulation into a self-consistent framework and provide assessment of the upscale impact of mesoscale fluctuations in a transparent fashion. Because of limited computing resources, present-day GCMs have too-coarse resolutions to explicitly resolve mesoscale fluctuations of flow fields during the ITCZ breakdown. The assessment of the upscale impact of mesoscale fluctuations by the M-ITCZ model can provide a simple way to parameterize the spatial pattern of the upscale impact without directly resolving the mesoscale dynamics. The M-ITCZ equations under the current model setup can also be generalized in several ways and used to model other phenomena in the ITCZ. For example, as suggested in Biello and Majda (2013), instead of prescribing the diabatic heating, an active heating coupling the M-ITCZ equations with moisture will introduce new realistic features of tropical flows. The resulting model should be useful to model the convective instability in the ITCZ and flow fields during the ITCZ breakdown. Also, it is interesting to consider the interaction between the ITCZ and a nearby tropical cyclone, particularly the influence of perturbation induced by tropical cyclone circulation on the ITCZ breakdown (Ferreira and Schubert 1997).

Acknowledgments. This research of A.J.M is partially supported by the Office of Naval Research ONR MURI N00014-12-1-0912, and Q.Y. is supported as a graduate research assistant on this grant and partially funded as a postdoctoral fellow by the Center for Prototype Climate Modeling (CPCM) in the New York University Abu Dhabi (NYUAD) Research Institute. The research of B.K. is partially supported by the Grant RGPIN 2015-04288 from the Natural Sciences and Engineering Research Council of Canada.

APPENDIX

Numerical Scheme

The M-ITCZ equations consist of two zonal spatial scales (planetary scale and mesoscale), and the corresponding dynamics on these scales are coupled to each other in complete nonlinearity. A suitable numerical scheme is required to simulate this model without violating the multiscale assumptions. The numerical scheme we used here shares many similar features with the so-called superparameterization

method (Majda and Grooms 2014), and it is split into two alternative steps. The first step is to solve the MEWTG equations in each mesoscale box, and the second step is to solve the planetary-scale gravity wave equations in the full domain.

Step 1: Solve the MEWTG equations in each single mesoscale box,

$$\frac{Du}{Dt} - yv = -\frac{\partial p}{\partial x} - du, \tag{A1a}$$

$$\frac{Dv}{Dt} + yu = -\frac{\partial p}{\partial y} - dv, \tag{A1b}$$

$$w = S_\theta, \tag{A1c}$$

$$\frac{\partial u}{\partial x} + \frac{\partial v}{\partial y} + \frac{\partial w}{\partial z} = 0, \tag{A1d}$$

and compute zonal and meridional averaging of u in each mesoscale box $\langle \overline{u} \rangle$.

Step 2: Solve the planetary-scale gravity wave equations,

$$\frac{\partial \langle \overline{u} \rangle}{\partial t} + \frac{\partial \Pi}{\partial X} = 0, \tag{A2a}$$

$$\frac{\partial \Pi}{\partial x} = \frac{\partial \Pi}{\partial y} = 0, \quad \frac{\partial \Pi}{\partial z} = \Theta, \tag{A2b}$$

$$\frac{\partial \Theta}{\partial t} + W = 0, \tag{A2c}$$

$$\frac{\partial}{\partial X}(\langle \overline{u} \rangle - U) + \frac{\partial W}{\partial z} = 0, \tag{A2d}$$

and update u in each mesoscale box by adding the increment of mean zonal velocity $\langle \overline{u} \rangle$.

a. *Solve the MEWTG equations in each single mesoscale box*

To solve the MEWTG equations, the Helmholtz decomposition is utilized to decompose horizontal velocity with streamfunction ψ and velocity potential ϕ,

$$u = -\frac{\partial \psi}{\partial y} + \frac{\partial \phi}{\partial x}, \tag{A3}$$

$$v = \frac{\partial \psi}{\partial x} + \frac{\partial \phi}{\partial y}, \tag{A4}$$

which turn out to be governed by two coupled Poisson's equations as follows ($\Delta = \partial^2/\partial x^2 + \partial^2/\partial y^2$):

$$\Delta \phi = -\frac{\partial}{\partial z} S_\theta, \tag{A5}$$

$$\Delta \psi = \xi, \tag{A6}$$

BC1: ϕ and ψ are periodic in x,

BC2: $\dfrac{\partial \psi}{\partial x} + \dfrac{\partial \phi}{\partial y} = 0 \quad \text{at} \quad y = \pm L_*$,

BC3: $-\dfrac{\partial \psi}{\partial y} + \dfrac{\partial \phi}{\partial x} = \overline{u} \quad \text{at} \quad y = \pm L_*$.

Such a technique is first used in Majda et al. (2010, 2008). Here, BC1 denotes the local periodicity boundary condition in the zonal direction. BC2 denotes rigid-lid condition for meridional velocity at the meridional boundaries. BC3 assumes the mesoscale fluctuations of zonal velocity vanish in the meridional boundaries $u' = 0$ and $u = \overline{u}$. Thus, the governing equation for mean zonal velocity at the meridional boundaries can be derived by taking the zonal average of Eq. (A1a):

$$\frac{\partial \overline{u}}{\partial t} + \overline{w} \frac{\partial \overline{u}}{\partial z} = -d\overline{u}. \tag{A7}$$

Besides, the vorticity is governed by a forced advection equation in three-dimensional flows,

$$\frac{\partial \xi}{\partial t} + u \frac{\partial \xi}{\partial x} + v \frac{\partial \xi}{\partial y} + w \frac{\partial \xi}{\partial z} = (\xi + y) \frac{\partial S_\theta}{\partial z} - \frac{\partial v}{\partial z} \frac{\partial S_\theta}{\partial x} + \frac{\partial u}{\partial z} \frac{\partial S_\theta}{\partial y} - v - d\xi, \tag{A8}$$

which is solved by a second-order corner transport upwind (CTU) scheme following LeVeque (2002) with careful treatment of corner flux terms to maintain second-order accuracy in space. In addition, the predictor–corrector scheme is utilized to improve temporal accuracy with two stages. A cheap first-order upwind scheme is implemented in the first stage. After estimating the velocity field at half time step in the first stage, the second-order piecewise linear CTU scheme is applied to calculate the vorticity in the second stage.

b. *Solve the planetary-scale gravity wave equations*

It is well known that such linear equations in Eqs. (A2a)–(A2d) with rigid-lid boundary conditions can be solved with explicit solution formulas in both barotropic and baroclinic modes (Majda 2003). In particular, the harmonic functions (sine and cosine functions) are a complete set of basis functions, which also satisfy the rigid-lid boundary conditions in the vertical direction. Thus, the linear planetary-scale gravity wave equations are solved through vertical mode decomposition with both the barotropic and baroclinic modes.

Case 1: Barotropic mode $q = 0$:

$$\frac{\partial U}{\partial t} + \frac{\partial \Pi_0}{\partial X} = 0, \tag{A9}$$

Here, the barotropic mode of pressure perturbation Π_0 is assumed to be constant for simplicity.

Case 2: Baroclinic modes $q > 0$:

$$\frac{\partial U_q}{\partial t} + \frac{\partial \Pi_q}{\partial X} = 0, \tag{A10a}$$

$$\Pi_q = \Theta_q, \tag{A10b}$$

$$\frac{\partial \Theta_q}{\partial t} + W_q = 0, \tag{A10c}$$

$$\frac{\partial U_q}{\partial X} - q^2 W_q = 0. \tag{A10d}$$

REFERENCES

Biello, J. A., and A. J. Majda, 2005: A new multiscale model for the Madden–Julian oscillation. *J. Atmos. Sci.*, **62**, 1694–1721, https://doi.org/10.1175/JAS3455.1.

——, and ——, 2006: Modulating synoptic scale convective activity and boundary layer dissipation in the IPESD models of the Madden–Julian oscillation. *Dyn. Atmos. Oceans*, **42**, 152–215, https://doi.org/10.1016/j.dynatmoce.2005.10.005.

——, and ——, 2010: Intraseasonal multi-scale moist dynamics of the tropical atmosphere. *Commun. Math. Sci.*, **8**, 519–540, https://doi.org/10.4310/CMS.2010.v8.n2.a11.

——, and ——, 2013: A multiscale model for the modulation and rectification of the ITCZ. *J. Atmos. Sci.*, **70**, 1053–1070, https://doi.org/10.1175/JAS-D-12-0142.1.

Bretherton, C. S., J. R. McCaa, and H. Grenier, 2004: A new parameterization for shallow cumulus convection and its application to marine subtropical cloud-topped boundary layers. Part I: Description and 1D results. *Mon. Wea. Rev.*, **132**, 864–882, https://doi.org/10.1175/1520-0493(2004)132<0864:ANPFSC>2.0.CO;2.

Deser, C., 1993: Diagnosis of the surface momentum balance over the tropical Pacific Ocean. *J. Climate*, **6**, 64–74, https://doi.org/10.1175/1520-0442(1993)006<0064:DOTSMB>2.0.CO;2.

Ferreira, R. N., and W. H. Schubert, 1997: Barotropic aspects of ITCZ breakdown. *J. Atmos. Sci.*, **54**, 261–285, https://doi.org/10.1175/1520-0469(1997)054<0261:BAOIB>2.0.CO;2.

Gill, A., 1980: Some simple solutions for heat-induced tropical circulation. *Quart. J. Roy. Meteor. Soc.*, **106**, 447–462, https://doi.org/10.1002/qj.49710644905.

Goswami, B., B. Khouider, R. Phani, P. Mukhopadhyay, and A. Majda, 2017: Improving synoptic and intra-seasonal variability in CFSv2 via stochastic representation of organized convection. *Geophys. Res. Lett.*, **44**, 1104–1113, https://doi.org/10.1002/2016GL071542.

Gray, W. M., 1979: Hurricanes: Their formation, structure, and likely role in the tropical circulation. *Meteorology over the Tropical Oceans*, D. B. Shaw, Ed., Royal Meteorological Society, 155–218.

Gu, G., and C. Zhang, 2002: Westward-propagating synoptic-scale disturbances and the ITCZ. *J. Atmos. Sci.*, **59**, 1062–1075, https://doi.org/10.1175/1520-0469(2002)059<1062:WPSSDA>2.0.CO;2.

Hack, J. J., W. H. Schubert, D. E. Stevens, and H.-C. Kuo, 1989: Response of the Hadley circulation to convective forcing in the ITCZ. *J. Atmos. Sci.*, **46**, 2957–2973, https://doi.org/10.1175/1520-0469(1989)046<2957:ROTHCT>2.0.CO;2.

Hubert, L., A. Krueger, and J. Winston, 1969: The double intertropical convergence zone—Fact or fiction? *J. Atmos. Sci.*, **26**, 771–773, https://doi.org/10.1175/1520-0469(1969)026<0771:TDICZF>2.0.CO;2.

Khouider, B., and A. J. Majda, 2008: Multicloud models for organized tropical convection: Enhanced congestus heating. *J. Atmos. Sci.*, **65**, 895–914, https://doi.org/10.1175/2007JAS2408.1.

——, Y. Han, and J. A. Biello, 2012: Convective momentum transport in a simple multicloud model for organized convection. *J. Atmos. Sci.*, **69**, 281–302, https://doi.org/10.1175/JAS-D-11-042.1.

Kuang, Z., and C. S. Bretherton, 2006: A mass-flux scheme view of a high-resolution simulation of a transition from shallow to deep cumulus convection. *J. Atmos. Sci.*, **63**, 1895–1909, https://doi.org/10.1175/JAS3723.1.

LeVeque, R. J., 2002: *Finite Volume Methods for Hyperbolic Problems*. Cambridge Texts in Applied Mathematics, Vol. 31, Cambridge University Press, 558 pp.

Lin, J.-L., 2007: The double-ITCZ problem in IPCC AR4 coupled GCMs: Ocean–atmosphere feedback analysis. *J. Climate*, **20**, 4497–4525, https://doi.org/10.1175/JCLI4272.1.

——, M. Zhang, and B. Mapes, 2005: Zonal momentum budget of the Madden–Julian oscillation: The source and strength of equivalent linear damping. *J. Atmos. Sci.*, **62**, 2172–2188, https://doi.org/10.1175/JAS3471.1.

Majda, A. J., 2003: *Introduction to PDEs and Waves for the Atmosphere and Ocean.* Courant Lecture Notes in Mathematics, Vol. 9, American Mathematical Society, 234 pp.

——, 2007: New multiscale models and self-similarity in tropical convection. *J. Atmos. Sci.*, **64**, 1393–1404, https://doi.org/10.1175/JAS3880.1.

——, and R. Klein, 2003: Systematic multiscale models for the tropics. *J. Atmos. Sci.*, **60**, 393–408, https://doi.org/10.1175/1520-0469(2003)060<0393:SMMFTT>2.0.CO;2.

——, and S. N. Stechmann, 2008: Stochastic models for convective momentum transport. *Proc. Natl. Acad. Sci. USA*, **105**, 17 614–17 619, https://doi.org/10.1073/pnas.0806838105.

——, and ——, 2009: A simple dynamical model with features of convective momentum transport. *J. Atmos. Sci.*, **66**, 373–392, https://doi.org/10.1175/2008JAS2805.1.

——, and I. Grooms, 2014: New perspectives on superparameterization for geophysical turbulence. *J. Comput. Phys.*, **271**, 60–77, https://doi.org/10.1016/j.jcp.2013.09.014.

——, and Q. Yang, 2016: A multiscale model for the intraseasonal impact of the diurnal cycle over the maritime continent on the Madden–Julian oscillation. *J. Atmos. Sci.*, **73**, 579–604, https://doi.org/10.1175/JAS-D-15-0158.1.

——, M. Mohammadian, and Y. Xing, 2008: Vertically sheared horizontal flow with mass sources: A canonical balanced model. *Geophys. Astrophys. Fluid Dyn.*, **102**, 543–591, https://doi.org/10.1080/03091920802044787.

——, Y. Xing, and M. Mohammadian, 2010: Moist multi-scale models for the hurricane embryo. *J. Fluid Mech.*, **657**, 478–501, https://doi.org/10.1017/S0022112010001515.

Mapes, B. E., and R. A. Houze Jr., 1993: Cloud clusters and superclusters over the oceanic warm pool. *Mon. Wea. Rev.*, **121**, 1398–1416, https://doi.org/10.1175/1520-0493(1993)121<1398:CCASOT>2.0.CO;2.

Moncrieff, M. W., C. Liu, and P. Bogenschutz, 2017: Simulation, modeling, and dynamically based parameterization of organized

tropical convection for global climate models. *J. Atmos. Sci.*, **74**, 1363–1380, https://doi.org/10.1175/JAS-D-16-0166.1.

Neggers, R. A., J. D. Neelin, and B. Stevens, 2007: Impact mechanisms of shallow cumulus convection on tropical climate dynamics. *J. Climate*, **20**, 2623–2642, https://doi.org/10.1175/JCLI4079.1.

Nolan, D. S., C. Zhang, and S.-H. Chen, 2007: Dynamics of the shallow meridional circulation around intertropical convergence zones. *J. Atmos. Sci.*, **64**, 2262–2285, https://doi.org/10.1175/JAS3964.1.

Philander, S., D. Gu, G. Lambert, T. Li, D. Halpern, N. Lau, and R. Pacanowski, 1996: Why the ITCZ is mostly north of the equator. *J. Climate*, **9**, 2958–2972, https://doi.org/10.1175/1520-0442(1996)009<2958:WTIIMN>2.0.CO;2.

Romps, D. M., 2014: Rayleigh damping in the free troposphere. *J. Atmos. Sci.*, **71**, 553–565, https://doi.org/10.1175/JAS-D-13-062.1.

Schneider, E. K., and R. S. Lindzen, 1977: Axially symmetric steady-state models of the basic state for instability and climate studies. Part I. Linearized calculations. *J. Atmos. Sci.*, **34**, 263–279, https://doi.org/10.1175/1520-0469(1977)034<0263:ASSSMO>2.0.CO;2.

Schneider, T., 2006: The general circulation of the atmosphere. *Annu. Rev. Earth Planet. Sci.*, **34**, 655–688, https://doi.org/10.1146/annurev.earth.34.031405.125144.

——, P. A. O'Gorman, and X. J. Levine, 2010: Water vapor and the dynamics of climate changes. *Rev. Geophys.*, **48**, RG3001, https://doi.org/10.1029/2009RG000302.

Sobel, A. H., J. Nilsson, and L. M. Polvani, 2001: The weak temperature gradient approximation and balanced tropical moisture waves. *J. Atmos. Sci.*, **58**, 3650–3665, https://doi.org/10.1175/1520-0469(2001)058<3650:TWTGAA>2.0.CO;2.

Toma, V. E., and P. J. Webster, 2010a: Oscillations of the intertropical convergence zone and the genesis of easterly waves. Part I: Diagnostics and theory. *Climate Dyn.*, **34**, 587–604, https://doi.org/10.1007/s00382-009-0584-x.

——, and ——, 2010b: Oscillations of the intertropical convergence zone and the genesis of easterly waves. Part II: Numerical verification. *Climate Dyn.*, **34**, 605–613, https://doi.org/10.1007/s00382-009-0585-9.

Trenberth, K. E., and D. P. Stepaniak, 2003a: Covariability of components of poleward atmospheric energy transports on seasonal and interannual timescales. *J. Climate*, **16**, 3691–3705, https://doi.org/10.1175/1520-0442(2003)016<3691:COCOPA>2.0.CO;2.

——, and ——, 2003b: Seamless poleward atmospheric energy transports and implications for the Hadley circulation. *J. Climate*, **16**, 3706–3722, https://doi.org/10.1175/1520-0442(2003)016<3706:SPAETA>2.0.CO;2.

Waliser, D. E., and C. Gautier, 1993: A satellite-derived climatology of the ITCZ. *J. Climate*, **6**, 2162–2174, https://doi.org/10.1175/1520-0442(1993)006<2162:ASDCOT>2.0.CO;2.

Wang, C.-C., and G. Magnusdottir, 2005: ITCZ breakdown in three-dimensional flows. *J. Atmos. Sci.*, **62**, 1497–1512, https://doi.org/10.1175/JAS3409.1.

——, and ——, 2006: The ITCZ in the central and eastern Pacific on synoptic time scales. *Mon. Wea. Rev.*, **134**, 1405–1421, https://doi.org/10.1175/MWR3130.1.

Wu, Z., 2003: A shallow CISK, deep equilibrium mechanism for the interaction between large-scale convection and large-scale circulations in the tropics. *J. Atmos. Sci.*, **60**, 377–392, https://doi.org/10.1175/1520-0469(2003)060<0377:ASCDEM>2.0.CO;2.

Wyrtki, K., and G. Meyers, 1976: The trade wind field over the Pacific Ocean. *J. Appl. Meteor.*, **15**, 698–704, https://doi.org/10.1175/1520-0450(1976)015<0698:TTWFOT>2.0.CO;2.

Yang, Q., and A. J. Majda, 2014: A multi-scale model for the intraseasonal impact of the diurnal cycle of tropical convection. *Theor. Comput. Fluid Dyn.*, **28**, 605–633, https://doi.org/10.1007/s00162-014-0336-3.

Zhang, C., 2001: Double ITCZs. *J. Geophys. Res.*, **106**, 11 785–11 792, https://doi.org/10.1029/2001JD900046.

——, M. McGauley, and N. A. Bond, 2004: Shallow meridional circulation in the tropical eastern Pacific. *J. Climate*, **17**, 133–139, https://doi.org/10.1175/1520-0442(2004)017<0133:SMCITT>2.0.CO;2.

——, D. S. Nolan, C. D. Thorncroft, and H. Nguyen, 2008: Shallow meridional circulations in the tropical atmosphere. *J. Climate*, **21**, 3453–3470, https://doi.org/10.1175/2007JCLI1870.1.